Australian Bushfire Emissions Result in Enhanced Polar Stratospheric Clouds

Srinivasan Prasanth[1,2], Narayana Sarma Anand[3], Kudilil Sunilkumar[4], Subin Jose[5], Kenath Arun[1], Sreedharan K. Satheesh[2,4,6], and Krishnaswamy K. Moorthy[2]

[1]Department of Physics and Electronics, Christ University, Bengaluru, Karnataka, India

[2]Divecha Centre for Climate Change, Indian Institute of Science, Bengaluru, Karnataka, India

[3]School of Earth, Environmental and Sustainability Sciences, Indian Institute of Science Education and Research Thiruvananthapuram, Kerala, India

[4]Centre for Atmospheric and Oceanic Sciences, Indian Institute of Science, Bengaluru, Karnataka, India

[5]Department of Physics, Newman College, Thodupuzha, Kerala, India

[6]DST-Centre of Excellence in Climate Change, Indian Institute of Science, Bengaluru, Karnataka, India

Correspondence: Prasanth S. (prasanthphy57@gmail.com)

Abstract

Extreme bushfire events amplify climate change by emitting greenhouse gases and destroying carbon sinks while causing economic damage through property destruction and even fatalities. One such bushfire occurred in Australia during 2019/2020, injecting large amounts of aerosols and gases into the stratosphere and depleting the ozone layer. While previous studies focused on the drivers behind ozone depletion, the bushfire impact on the polar stratospheric clouds (PSC), a paramount factor in ozone depletion, has not been extensively investigated so far. This study focuses on the effects of bushfire aerosols on the dynamics and stratospheric chemistry related to the PSC formation and its pathways. An analysis from Aura's microwave limb sounder revealed enhanced hydrolysis of dinitrogen pentoxide significantly increased nitric acid (HNO_3) in the high-latitude lower stratosphere in early 2020. It resulted in anomalous high areal coverage of PSC with ice exceeding three standard deviations with respect to background period. Based on Lagrangian backward trajectory analysis, we report that 79 % and 21 % of liquid–Nitric Acid Trihydrate (NAT) mixture formed via ice-free and ice-assisted formation pathways respectively, and 95 % of ice formed via nucleating on NAT and rest on Supercooled Ternary Solution (STS) with possible inclusion of foreign nuclei. This highlights the primary formation pathways of ice and liquid–NAT mixtures and possibly helps us to simulate the PSC formation and denitrification process better in climate models. These findings will contribute significantly to a deeper understanding of the impacts of extreme wildfire events on stratospheric chemistry and PSC dynamics.

Keywords: Aerosols; Australian Bushfire; Formation pathways; Polar Stratospheric Clouds; Stratospheric chemistry

1 Introduction

Southeast Australia, comprising the states of New South Wales and Victoria, faced an extreme bushfire event from September 2019 to February 2020, which is widely recognized as the black summer or Australian New Year (ANY) event and has been extensively studied (Allen et al., 2020; Deb et al., 2020; Schwartz et al., 2020; Chang et al., 2021; Rieger et al., 2021; Tencé et al., 2021, 2022; Heinold et al., 2022; Sellitto et al., 2022). This catastrophic event injected substantial amounts of aerosols, between 0.4 and 2 Tg, into the southern hemispheric lower stratosphere (Khaykin et al., 2020; Hirsch and Koren, 2021; Heinold et al., 2022; Tencé et al., 2022); which composed of 2.5 % black carbon and 97.5 % organic carbon (Yu et al., 2021). Significant warming of the mid-latitude stratosphere by up to 3.5 K has been reported, which is unparalleled since the 1991 eruption of Mount Pinatubo (Stocker et al., 2021). Additionally, this event led to significant changes in the abundance of various trace gas species, such as CH_4, CO, CH_3CN, CH_3Cl, HCN, CH_3OH, HCl, HNO_3, H_2O, and $ClONO_2$, particularly in the mid-latitude lower stratosphere (Schwartz et al., 2020; Santee et al., 2022; Wang et al., 2023).

Furthermore, these aerosols provided a surface area for heterogeneous chlorine activation reactions to occur, resulting in the early depletion of HCl and an enhancement of ClO (Santee et al., 2022), and led to additional stratospheric ozone loss (Solomon et al., 2022). Along with these aerosols, liquid Polar Stratospheric Clouds (PSCs) are also known to promote such ozone-depleting heterogeneous reactions (Molina et al., 1993; Carslaw et al., 1994; Ravishankara and Hanson, 1996). Solid PSCs such as Nitric Acid Trihydrate (NAT) are known to retard the deactivation process of active halogens like chlorine, bromine, and fluorine through denitrification and thereby contribute to prolonged ozone depletion (Hoyle et al., 2013). Ansmann et al. (2022) reported that the bushfire aerosols from the black summer event have influenced the PSCs by increasing their surface area and particle number concentration. Wang et al. (2023) reported an increased stratospheric chlorine activation on the bushfire aerosols and PSCs. However, previous studies have not extensively investigated the influence of the black summer event on the PSC dynamics, particularly the formation pathways. It is crucial to understand the influence of extreme events like the black summer on PSC dynamics for two main reasons:

(i) The frequency of extreme wildfire events is projected to increase due to global warming (Mansoor et al., 2022), resulting in more injection of aerosols into the stratosphere, which could enhance the PSC area coverage.

(ii) Stratospheric cooling is anticipated to further expand the PSC coverage, resulting in more surface area density for chlorine activation reactions and thus more ozone depletion (e.g., Khosrawi et al., 2016; Thölix et al., 2016; Robrecht et al., 2019).

Under the above backdrop, using multi-satellite measurements and reanalysis data, this study aims to investigate the anomalies in stratospheric chemistry and PSC dynamics caused by the black summer event. In this paper, we first review the polar stratospheric clouds and their formation pathways relevant to the current study in Sect. 2. The data and methodology used in this study are detailed in Sect. 3. The results and their discussion are given in Sect. 4, and the study is concluded in Sect. 5.

2. Brief literature review of polar stratospheric clouds

The stratosphere contains a widespread presence of sulfate aerosols composed of sulfuric acid and water (Junge et al., 1961). It receives an influx of 160 tons of sulfur per day from the troposphere, which corresponds to the production of 650 tons per day of aqueous sulfuric acid (Thomason and Peter, 2006). In addition to the sulfate aerosols, meteoritic dust particles of extraterrestrial origin contribute 20-100 tons per day (Cziczo et al., 2001), making up 3–15% of the total mass of stratospheric aerosols. These dust particles are carried by the Brewer-Dobson circulation and funneled from the mesosphere into the stratospheric polar regions of both hemispheres during the formation of the polar vortex (Engel et al., 2013). As winter approaches, the absence of solar radiation in the polar regions leads to a significant decrease in temperature, creating conditions conducive for trace gases such as HNO_3 and H_2O to condense onto the stratospheric aerosols, forming polar stratospheric clouds (PSCs) (Carslaw et al., 1994; Voigt et al., 2000). Hence, these PSC particles predominantly consist of HNO_3, H_2SO_4, and H_2O (Lowe and MacKenzie, 2008; Peter, 1997). It is hypothesized that stratospheric sulfuric acid aerosols containing meteoritic dust could also serve as the nuclei for PSC formation (Bogdan et al., 2003; Bogdan and Kulmala, 1999; Murphy et al., 2014; Schneider et al., 2021).

2.1 Types of PSC

The PSCs exist in both liquid and solid form in the lower stratosphere. The Supercooled Ternary Solution (STS) is liquid PSC with an equal proportion of H_2SO_4, HNO_3, and H_2O which forms at T_{ice} + 3 K (Carslaw et al., 1994). The Nitric Acid Trihydrate (NAT) are solid particles with a proportion of 1 HNO_3 and 3 H_2O and form at T_{ice} + 4 K (Hanson and Mauersberger, 1988). Furthermore, ice PSC forms through homogeneous nucleation at T_{ice} – 3 K (Carslaw et al., 1998; Koop et al., 1998), and heterogeneous nucleation of ice at T_{ice} – 0.1 to 1.5 K (Koop et al., 1998, 2000; Fortin et al., 2003; Engel et al., 2013). The STS assists in chlorine activation by providing surface area resulting in pronounced ozone depletion and NAT is involved in denitrification leading to prolonged ozone depletion (Molina and Rowland, 1974; Molina et al., 1993; Ravishankara and Hanson, 1996; Waibel et al., 1999; Hoyle et al., 2013).

2.2 PSC formation pathways

2.2.1 NAT formation pathways

The homogeneous nucleation of NAT is kinetically suppressed (Koop et al., 1995). Laboratory experiments have revealed that the homogeneous nucleation rate of NAT on liquid STS is extremely low for stratospheric conditions (Hanson and Ravishankara, 1991, 1992). Thus, NAT forms through heterogeneous nucleation processes such as (i) ice–assisted NAT nucleation and (ii) ice-free NAT nucleation. During the ice–assisted NAT nucleation process, the ice particles serve as nuclei for NAT formation upon warming of the air parcels and it occurs at a high saturation ratio over NAT of > 500 (Luo et al., 2003). This mechanism has been supported by several field observations (Carslaw et al., 1999) and by bulk phase lab experiments (Koop et al., 1995, 1997) indicating that deposition nucleation of NAT on exposed ice surfaces is also a possible pathway for NAT formation. During the ice-free NAT nucleation, instead of ice, STS with inclusion of solid foreign nuclei such as meteoritic dust, volcanic

ash, soot, or H_2SO_4 hydrates serve as NAT nuclei (Iraci et al., 1995; Koop et al., 1997; Peter and Grooß, 2012) and it occurs even at the low saturation ratio over NAT (S_{NAT}) of < 10 (Voigt et al., 2005). Hoyle et al., (2013) made a new parameterization scheme for NAT nucleation on foreign nuclei in immersion mode and reproduced the CALIPSO PSC observation for the entire Arctic winter of 2009/2010.

2.2.2 Ice formation pathways

The ice PSC can form either homogeneously under high supersaturation conditions of saturation ratio over ice (S_{ice}) >1.5 and at temperature 3 K less than the frost point (T_{ice}) (Koop et al., 1998) or heterogeneously on STS with foreign nuclei inclusion at temperature 1.5 K less than T_{ice} (Koop et al., 1998, 2000; Engel et al., 2013). Apart from these foreign nuclei, NAT is also known to act as potential nuclei for ice formation (Gao et al., 2016; Hanson and Mauersberger, 1988; Iannarelli and Rossi, 2015; Khosrawi et al., 2011; Weiss et al., 2016). Based on WALES (Water Vapor Lidar Experiment in Space – airborne demonstrator) lidar on board the HALO (High Altitude and Long Range Research Aircraft), Voigt et al., (2018) showed that the depolarization ratio of ice PSC exhibited bimodal distribution where low depolarization mode corresponds to the ice nucleated on STS with foreign nuclei inclusion and high depolarization mode to the ice nucleated on NAT particle. Engel et al., (2013) made a new parameterization scheme for ice nucleation on foreign nuclei in immersion mode and reproduced the CALIPSO PSC observation for the entire Arctic winter 2009/2010.

In the present study, along with investigating the impact of the black summer event on lower stratospheric chemistry, we also aim to quantify the percentage of the liquid-NAT mixture formed via the ice-assisted and ice-free nucleation process. Further, we quantify the percentage of ice PSC which nucleates on NAT (NAT-assisted nucleation pathway), and STS (NAT-free nucleation pathway).

3 Data and Methodology

3.1 Satellite and reanalysis data

Ozone Monitoring Profiler Suite (OMPS) on board Suomi NPP and NOAA-20 satellites measures atmospheric O_3 and aerosols using limb viewing techniques. We have used OMPS level 2 version 2.0 product which provides aerosol extinction coefficient at 745 nm wavelength, with a horizontal resolution of 125 km × 2 km and a vertical resolution of 1.8 km (https://disc.gsfc.nasa.gov/datasets/OMPS_NPP_LP_L2_AER_DAILY_2/summary; Taha et al., 2021).

Microwave Limb Sounder (MLS) aboard the Aura satellite provides trace gas mixing ratios by measuring limb emission spectra through a 5-band microwave radiometer. We have used the MLS Level 2, version 5.0 daily HNO_3 and H_2O mixing ratios(https://mls.jpl.nasa.gov/eos-aura-mls/data-products; Waters et al., 2006) for the present study.

Atmospheric Chemistry Experiment-FTS (ACE-FTS) onboard SciSat satellite provides trace gases mixing ratio by measuring limb absorption spectra and level 2, version 4.0 daily HF, H_2O, HNO_3, N_2O_5 mixing ratio (https://www.frdr-dfdr.ca/repo/dataset/c75d2c49-0def-49e5-9c69-5e74c824dc6c; Bernath et al., 2020).

Cloud-Aerosol Lidar with Orthogonal Polarization (CALIOP) onboard Cloud-Aerosol Lidar and Infrared Pathfinder Satellite Observations (CALIPSO) satellite probes the vertical distribution of aerosols and clouds (Pitts et al., 2007). It classifies the PSCs through perpendicular attenuated backscatter and total scattering ratio (ratio between the total attenuated backscatter to the molecular backscatter), into five categories: Supercooled Ternary Solution (STS ≡ $H_2SO_4.HNO_3.H_2O$), Liquid-Nitric Acid Trihydrate mixtures (liquid-NAT mixtures ≡ $HNO_3.3H_2O$, a mixture of liquid STS and solid NAT with low number density of 10^{-2} cm^{-3}), enh. NAT (Enhanced NAT, with a high number density of 10^{-1} cm^{-3}), Ice (Water ice ≡ H_2O), and Mountain Wave Ice (MWI ≡ H_2O, caused by gravity waves). The total areal coverage of the PSCs such as liquid—NAT mixtures, STS, Ice, enh. NAT and MWI contribute 48 %, 24.7 %, 21.4 %, 5.8 %, and 0.1 % respectively (Pitts et al., 2018). However, these values are subject to interannual variation, modulated by the polar vortex dynamics. In addition, gas-phase HNO_3 is observed from Microwave Limb Sounder (MLS) from March to April every year. The backscattered signals from the sub-visible PSCs, which are NAT particles with extremely low number density, are well below the detection threshold of the CALIPSO receiver. Hence CALIPSO classifies these grids as 'No Cloud (NC)' (Lambert et al., 2012) during this period. Thus, the CALIPSO NC grid indicates either no presence of PSCs or the presence of sub-visible PSCs. In this study, CALIPSO PSC Level 2, version 2.0 is used (https://asdc.larc.nasa.gov/project/CALIPSO/CAL_LID_L2_PSCMask-Standard-V2-00_V2-00; Pitts et al., 2007; 2009; 2013), which provides PSC information at a spatial resolution of 180 m along the flight track and 500 m perpendicular to the track. The PSC areal coverage is estimated as described in Pitts et al. (2009).

European Centre for Medium-Range Weather Forecasts Reanalysis fifth generation (ERA-5) reanalysis provides meteorological data with a spatial resolution of 0.25° × 0.25° and a temporal resolution of 1 hour at 37 pressure levels (1000 to 1 hPa). We have used the hourly meridional and zonal velocity from June 2020 to July 2020 (https://cds.climate.copernicus.eu/cdsapp#!/dataset/reanalysis-era5-pressure-levels?tab=overview; Hersbach et al., 2020).

3.2 Anomaly estimation

Anomalies (Δ) in aerosol extinction coefficient (k_{ext} at 745 nm), mixing ratios of H_2O, and HNO_3, and PSC properties (such as areal coverage and volume) are estimated following Eq. (1):

$$\Delta X = X_{2020} - \bar{X} \quad (1)$$

where 'ΔX' is a daily anomaly of quantity 'X', 'X_{2020}' is the daily mean in 2020, and '$\bar{X}$' is the daily background mean. The background mean values of H_2O and HNO_3 mixing ratio and PSC properties are constructed by averaging the daily values during the period 2009 to 2019 while for k_{ext}, the period is 2012 to 2019 [excluding the year 2015, to avoid the effects of the Calbuco volcanic eruption (Zhu et al., 2018)]. The standardized anomaly (Z) is estimated following Eq. (2):

$$Z_X = \frac{\Delta X}{\sigma_X} \quad (2)$$

where 'σ_X' is the standard deviation of the parameter 'X'.

3.3 Methodology for retrieval of formation pathways

To retrieve the formation pathways of the PSCs, knowledge of the temperature history of the corresponding air parcel is crucial (Larsen et al., 1997). Hence, using the CLaMS trajectory module, the backward trajectories of the air parcels containing ice and liquid NAT mixture PSCs are calculated. The methodology is similar to the previous studies which retrieved the PSC formation pathways from CALIPSO (Nakajima et al., 2016) and from aircraft campaigns (Voigt et al., 2018) using Lagrangian trajectory analysis. The current methodology employed in this paper has three steps: (i) Selection of ice and liquid NAT mixture PSCs, (ii) Lagrangian backward trajectory analysis, and (iii) Determining the change in PSC composition. These three steps are described below.

(i) Selection of ice and liquid-NAT mixture PSCs:

Since liquid-NAT mixture and ice are the first (with 48 %) and third (with 21.4 %) most abundant types of PSCs in terms of areal coverage (Pitts et al., 2018), performing backward trajectories for all these detected PSC types is computationally expensive. Furthermore, The ERA5 operational analysis data are available at the temporal resolution of 1 hr. Whereas, the CALIPSO's temporal resolution is 1 profile sec^{-1}. The accuracy of the trajectory relies on the accuracy of the wind field and diabatic heating rate. Hence, assigning hourly wind field and diabatic heating rate to all CALIPSO profiles measured during the specific hour may contribute to uncertainty in the calculated trajectory. Though the degree of uncertainty is unclear, as a conservative measure, we impose another criterion to minimize any uncertainty which may contribute.

Criteria 1: Firstly, CALIPSO profiles which are measured within 5 minutes before and after (i.e., the 10-minute time windows) of any hours of ERA5 operational analysis are chosen. For instance, if ERA5 operational analysis data is available for the time 01:00 UTC for a specific day, CALIPSO profiles which are measured between 12:55 UTC and 01:05 UTC on the same day are considered.

Criteria 2: Secondly, from these chosen profiles, an ice PSC (liquid-NAT mixture PSC) grid is chosen only if all its surrounding grids are classified as ice PSC (liquid-NAT mixture PSC) i.e., the CALIPSO grids of size 3x3 should be homogeneously populated by either ice or liquid-NAT mixture.

(ii) Lagrangian backward trajectory analysis:

The backward trajectories for these selected grid points are calculated for a 48 h period using the CLaMS trajectory module. The rationale behind choosing the 48 h is that once the air parcel's temperature drops below T_{NAT} and following the nucleation of NAT particles with a number density of 5×10^{-4} to 5×10^{-5} cm^{-3}, within ~19 h (0.8 day) the NAT particles exceed CALIPSO perpendicular backscatter threshold and becomes detectable (Lambert et al., 2016). Similarly, Voigt et al., (2005) provided observational evidence from aircraft campaigns showing NAT formation within approximately 20 hours after the temperature drops below $T_{NAT.}$ In the case of ice formation, the 48 h period should be sufficient while considering the average cooling rate of the stratosphere. The model runs are driven by meteorological data from the ERA5 operational analysis, with a temporal resolution of 1 hour and a spatial resolution of 1° x 1°. The timestep is set to 60 seconds in the CLaMS trajectory module. The vertical coordinate is in potential temperature. The vertical motion of the air parcels is modulated by total diabatic heating rates derived from ERA5 as followed by Ploeger et al., (2021).

(iii) Determining the change in PSC composition

To determine the PSC composition along each trajectory, we first identify the intersection points where the trajectory intersects with the CALIPSO scan track, with a temporal coincidence of ±30 minutes. Intersections with time differences exceeding this threshold are disregarded, ensuring that the trajectory and CALIPSO scan track are both spatially and temporally co-located within a 30-minute time window. The PSC composition at each trajectory intersection point is then determined from the CALIPSO measurement profile with a potential temperature closest to that of the trajectory's intersecting point. If the determined PSC composition in this manner differs from the initial composition observed at the start of the trajectory (i.e., at time t = 0 h), we assign this PSC composition to the intersection point of the trajectory. Conversely, trajectories with no change in PSC composition are excluded from further consideration. Also, we fill the MLS observed HNO_3, and H_2O mixing ratio along the selected trajectories to study the uptake of these gases during PSC formation.

Following the above three steps, we chose a total of 8,841 backward trajectories. Out of these, 3792 trajectories correspond to the liquid-NAT mixture, and the rest 5049 trajectories to ice PSC. Each trajectory contains temperature from ERA5 operational analysis, HNO_3, and H_2O mixing ratio from MLS at the points where the trajectories intersect with CALIPSO scan track, and PSC composition from CALIPSO. In addition, derived quantities such as T_{ice}, T_{NAT}, ice and NAT surface area density from CLaMS box model run, S_{NAT} (for the case of backward trajectories of liquid-NAT mixture), and S_{ice} (for the case of backward trajectories of ice) are added to the trajectories. Hence, this provides a comprehensive picture of the air parcels' temporal evolution leading to the formation of liquid-NAT mixture and ice PSCs.

3.4 CLaMS microphysical modelling of observed uptakes of HNO_3 and H_2O

During the formation of ice and liquid-NAT mixture PSCs, uptake of gas-phase HNO_3, and H_2O mixing ratio occurs. We used the Chemical Lagrangian Model of the Stratosphere (CLaMS) microphysical box model to validate the MLS observed uptake in these gases with CLaMS-modeled uptake during the formation of the PSCs. CLaMS is a chemical transport model developed by Research Centre Jülich, Germany (McKenna et al., 2002a, b). It has several modules such as chemistry (McKenna et al., 2002b), mixing (McKenna et al., 2002a), trajectory (Konopka et al., 2004), sedimentation (Grooß et al., 2005, 2014; Tritscher et al., 2019), etc. which collectively helps in simulating simulate stratospheric chemistry, PSC formations, and ozone depletion.

In the present study, we utilized the trajectory module and microphysical box model from the chemistry module. First, a backward trajectory is estimated as discussed in Sect 3.3 (ii), and the intersection of the trajectory with the CALIPSO scan track is identified as discussed in Sect 3.3 (iii). Since the CALIPSO PSC product comes with MLS observations interpolated to the CALIPSO grids, the beginning and end of the trajectory have MLS HNO_3 and H_2O. Intersection of the backward trajectory with the CALIPSO scan track is considered as a beginning point and fed into the CLaMS microphysical box i.e., the trajectory starts at time, $t < 0$ hr and ends at time = 0 hr. The inputs for the box model run are trajectory coordinates (time, latitude, longitude, and potential temperature), temperature and pressure along the trajectories, and MLS observed HNO_3 and H_2O mixing ratio at the beginning of the trajectory. The mixing ratios of the rest of the gases are set to '0', hence other chemical reactions such as chlorine activation, HCl null cycles, and N_2O_5 hydrolysis are not considered. In the box model run, T_{ice} is estimated following equations provided by (Marti and Mauersberger, 1993), and T_{NAT} is estimated following (Hanson and Mauersberger, 1988).

4 Results and discussions

4.1 Increased aerosol loading in the lower stratosphere

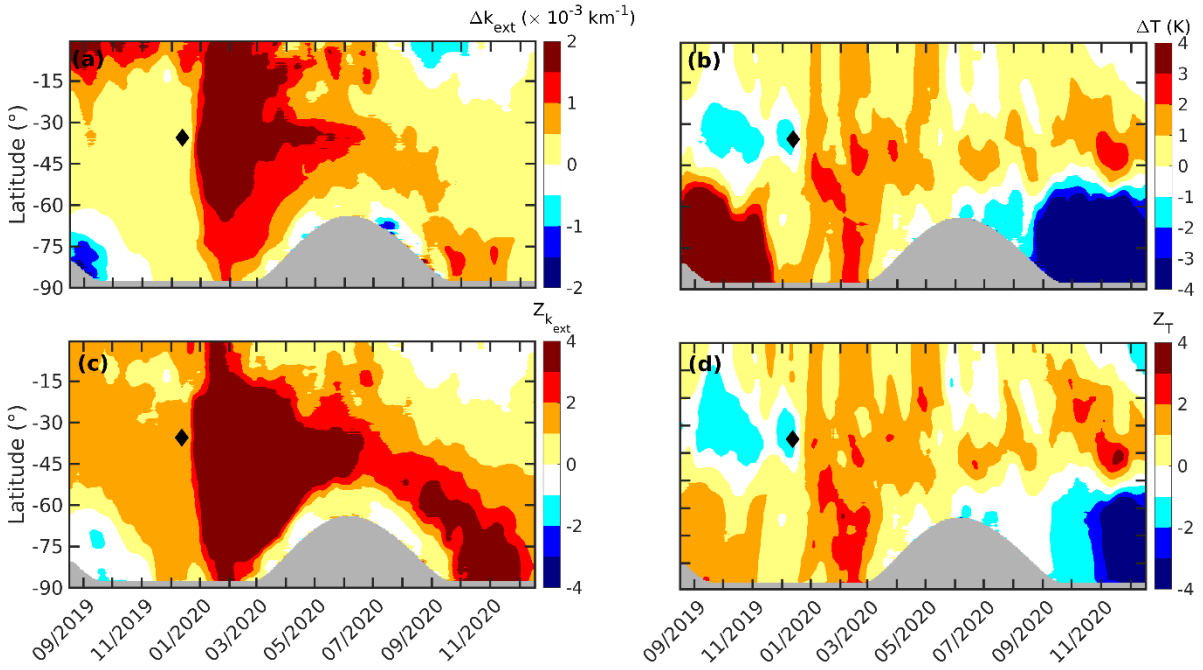

Figure 1: Daily zonal mean anomaly (Δ) in OMPS (a) k_{ext} at 745 nm, (b) temperature, and standardized anomaly (Z) of (c) k_{ext} at 745 nm and (d) temperature at the altitude of 15 km between September 2019 and December 2020 are shown. The grey-shaded region corresponds to no data. The x-ticks mark the middle of each month. The black diamond in each plot marks the black summer event.

An anomaly in aerosol extinction coefficient (k_{ext}) at 745 nm derived from cloud-filtered OMPS observations, and temperature along with their corresponding standardized anomalies at the altitude of 15 km are shown in Fig. 1. A notable positive anomaly of k_{ext} in mid-latitude since early January 2020 is attributable to the increased aerosol loading caused by the black summer event (Fig. 1a). The anomaly in k_{ext} exceeded three standard deviations (Fig. 1c) and warmed the lower stratosphere by 2 K owing to the radiative heating (Rieger et al., 2021), which is readily seen in Fig. 1b. By February 2020, these aerosols have been transported to high latitudes where PSC usually forms in the subsequent Austral winter. As stratospheric aerosols act as nuclei for PSC, it is likely that these aerosols also influenced the PSC dynamics during this period. A negative anomaly of k_{ext} has been observed at the latitude ~-80° since April 2020, which is attributed to the nucleation of PSC on these aerosols (Zhu et al., 2018). The k_{ext} increased again at high latitudes in October and November 2020 due to the re-release of the captured aerosols by the PSC, upon evaporation of the corresponding gas species (Toon et al., 1989; Schwarzenböck et al., 2001; Rex et al., 2004; Hoyle et al., 2013). Previous studies reported additional ozone loss during the same period (Ansmann et al., 2022; Ohneiser et al., 2022). Despite the abundant aerosol loading, strong cooling of more than 3 K is observed at high latitude regions from September to December 2020 (Fig. 1b). This suggests that the radiative cooling caused by the additional ozone loss (Fig. S1) has surpassed the radiative heating by the increased aerosol

loading, in agreement with Rex et al., (2004). Before the black summer event, intense warming exceeding 5 K was observed at the high latitude of the lower stratosphere from September to November 2019, which was attributed to a minor sudden stratospheric warming event (Liu et al., 2022).

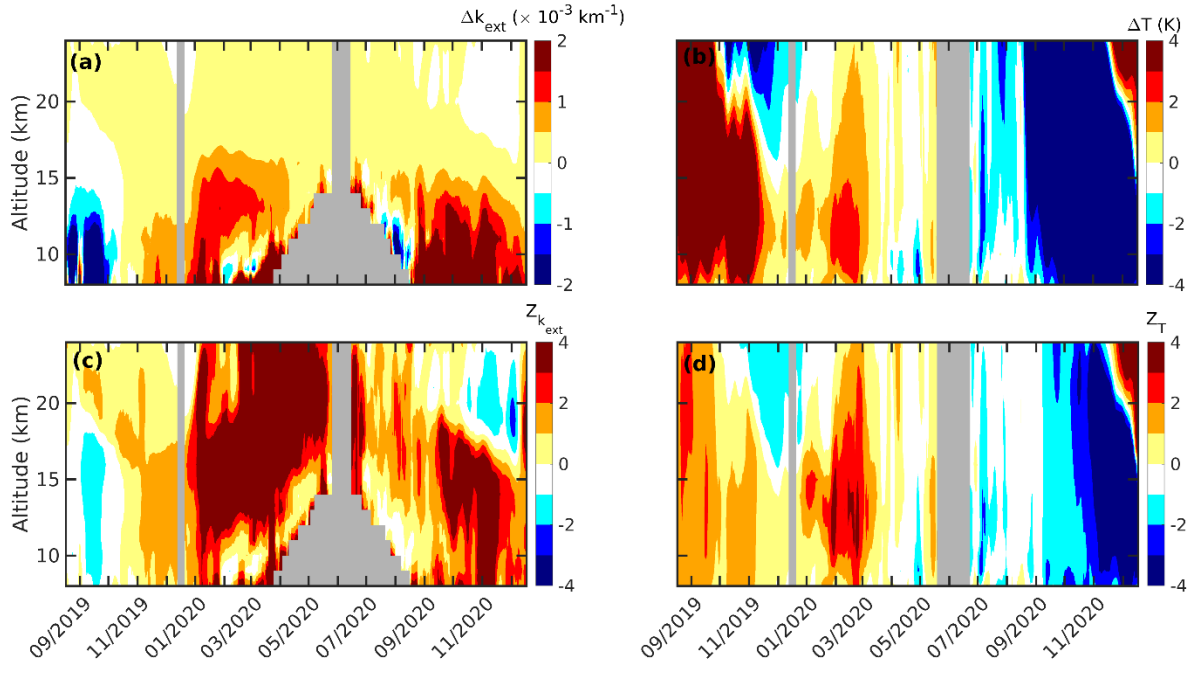

Figure 2: Daily vertical anomaly (Δ) in OMPS (a) k_{ext} at 745 nm, (b) temperature, and standardized anomaly (Z) of (c) k_{ext} at 745 nm and (d) temperature averaged between latitude -60° and -90° from September 2019 to December 2020 are shown. The grey-shaded region corresponds to no data. The x-ticks mark the middle of each month. The black diamond in each plot marks the black summer event.

The vertical profiles of anomaly and standardized anomaly (Z) of k_{ext} and temperature are shown in Fig. 2. Significant aerosol loading is observed as shown in Fig. 2a between the altitudes of 10 to 25 km from January to June 2020. The continuous increase in Z_{kext} since January 2020, to an even higher altitude (Fig. 2c), is attributed to the self-lofting mechanism (Khaykin et al., 2020). Like Fig. 1, the positive anomaly in k_{ext} in the lower stratosphere from October to December 2020 surpassed the anomaly observed during early 2020. The major type of aerosol emitted during the black summer is organic carbon (Yu et al., 2021), which is hydrophilic in nature. The increased k_{ext} could hence be due to the exposure of these aerosols in the low temperatures during the winter where condensation of water vapor resulted in the growth of the aerosols, increasing its size and light extinction further. In addition, the transport of more bushfire aerosols from mid to high–latitude regions could be another cause of the observed increase in Δk_{ext}. The descending pattern as observed in Z_{kext} (Fig. 2c) from August to December 2020 could be due to the result of the descent of the mesospheric air, as explained by Kessenich et al. (2023).

The OMPS does not provide information about the aerosols during polar winter due to lack of solar radiation which can be seen through grey shaded region in Fig. 1 and Fig. 2. Hence, the total attenuated backscatter (β) at

532 nm measured by CALIPSO for grids classified as 'No Cloud (NC)' at temperatures above the equilibrium temperature of NAT particles (T_{NAT}) are chosen to study the influence of the black summer event on lower stratospheric aerosol during the Austral winter 2020 at high latitude region (Fig. S3). Since the total attenuated backscatter is above T_{NAT}, it could correspond to the lower stratospheric aerosols, thus excluding the influence of sub-visible PSCs or PSCs. From May to mid-June 2020, the total attenuated backscatter varies between 1.6×10^{-4} and 1.8×10^{-4} (km^{-1} Sr^{-1}) which is more than one standard deviation with respect to the background mean (Fig. S3). After mid-June 2020, the total attenuated backscatter value has returned to its background level.

These observations reveal high aerosol loading in the lower stratosphere of the high latitudes after the black summer event. It can increase the surface area availability for heterogeneous chemical reactions and potentially modify the stratospheric chemistry itself. For a comprehensive understanding of the impact of the black summer event on the PSC dynamics, we explore the changes in key constituent gases of PSCs in the next section.

4.2 Enhanced HNO_3 and H_2O in the lower stratosphere

The anomalies in MLS HNO_3 and H_2O mixing ratios along with their corresponding standardized anomalies averaged between latitudes -60° and -90° are shown in Fig. 3. An elevated level of HNO_3 mixing ratio has been observed between 20 to 30 km altitude since February 2020 and peaked by 1.5 ppb over the background value by April 2020 (Fig. 3a). This surge exceeded two standard deviations and remained significant till June 2020 at the altitude of 20 km (Fig. 3c). Similarly, an increase in the H_2O mixing ratio is observed at slightly lower altitudes (between 15 to 20 km) since mid-January 2020 (Fig. 3b), which exceeded more than one standard deviation (the cause of this anomalous increase is discussed in Sect. 4.3). As both HNO_3 and H_2O are principal constituents of the PSCs (Tabazadeh et al., 1994; Voigt et al., 2000; Höpfner et al., 2006; Tritscher et al., 2021), the near-simultaneous decrease of them along with k_{ext} (Fig. 2a, and Fig. S3) during Austral winter suggests that these species condensed on the bushfire aerosols and thus likely converted into PSCs.

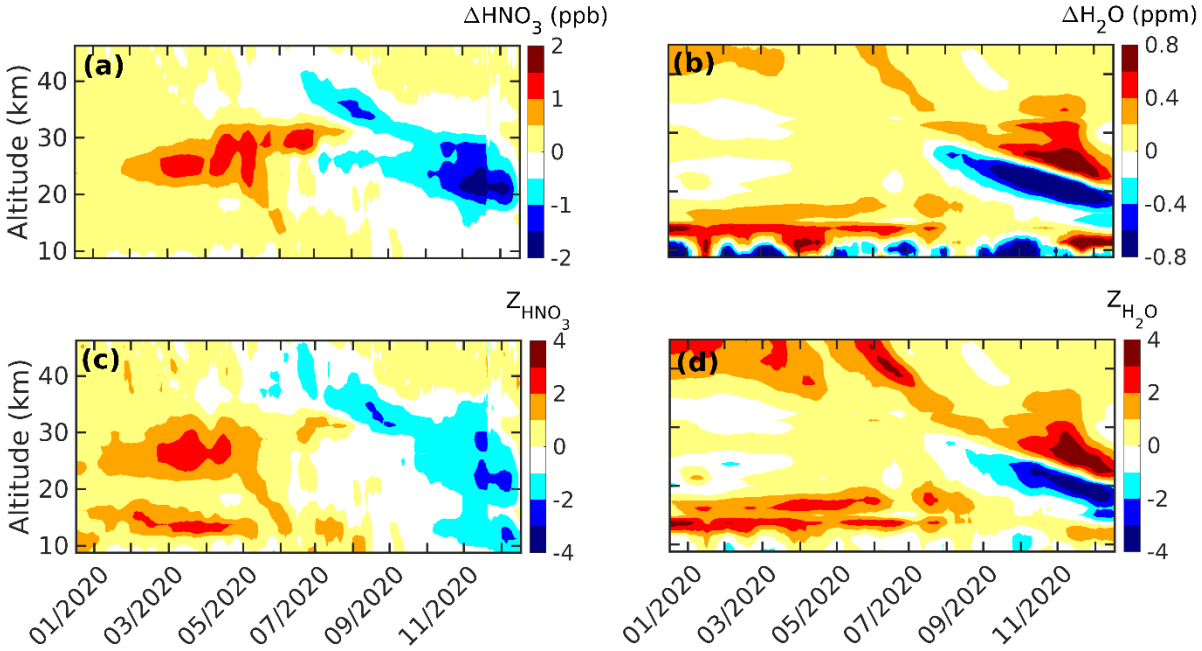

Figure 3: Anomaly in (a) HNO_3 and (b) H_2O mixing ratio, and standardized anomaly of (c) HNO_3 and (d) H_2O mixing ratio, averaged between latitudes -60° and -90° during 2020. The x-ticks mark the middle of each month.

Unlike HNO_3, abundant water vapor is detected in the upper stratosphere (above 40 km) (Fig. 3b and d) from January to April 2020. Since there is no evidence that the smoke plume from the black summer event has reached such altitudes, we believe that the moist upper stratosphere is not associated with the black summer event. The upper stratospheric water vapor is produced through the oxidation of methane CH_4 (Brewer, 1949; Fueglistaler et al., 2009) and directly injected from the tropical tropopause layer through deep convection (Schoeberl et al., 2018). This water vapor is further transported from low to high latitudes through a deep branch (present at the upper and middle stratosphere) and a shallow branch (present just above tropopause) of the Brewer-Dobson circulation (Butchart, 2014). The descent of water vapor from the upper stratosphere to the lower stratosphere during 2020 shown in Fig. 3b suggests that these water vapors are carried by the deep branch of the Brewer-Dobson circulation and resulted in a strong positive H_2O anomaly from September to December 2020 within the altitudes of 30 to 25 km. A strong negative anomaly in both HNO_3 and H_2O can be observed below this layer during early 2020, which could be due to the prolonged polar vortex during this period separating the mid and high-latitude air mass, thereby preventing further mixing (Rieger et al., 2021; Klekociuk et al., 2022; Santee et al., 2022b; Yook et al., 2022). To understand whether the cause of these anomalies was due to dynamical (i.e. due to change in transportation) or chemical (i.e., due to chemical reaction) processes, a tracer-tracer correlation analysis was carried out and the results are discussed in the next section.

4.3 Tracer-Tracer Correlation Analysis

The Tracer-tracer correlation analysis technique is used to diagnose whether a change in atmospheric gas concentration is driven by chemical reactions or transportation (such as convection or advection). The idea behind this technique is that chemically active and long-lived trace (i.e., chemically inert) gas should exhibit the same order of change if the cause is transport-related (e.g., Müller et al., 1996, 1997). If a chemically active gas increases/decreases with no change in long-lived trace gas, that change is attributed to the chemical reaction. In this technique, a linear regression between the long-lived trace gas and the chemically active gas is performed for both during the background periods (in this study, March 2009–2019). A deviation of the data corresponding to the period of interest (March 2020; red diamond in Fig. 4 (a)) from the regression line indicates the chemical production of the chemically active gases. Likewise, an alignment with the regression line indicates the transport-related cause of the chemically active gases. For our analysis, hydrofluoric acid (HF) was chosen as the long-lived trace gas, as it is chemically inert in the stratosphere (Wang et al., 2023).

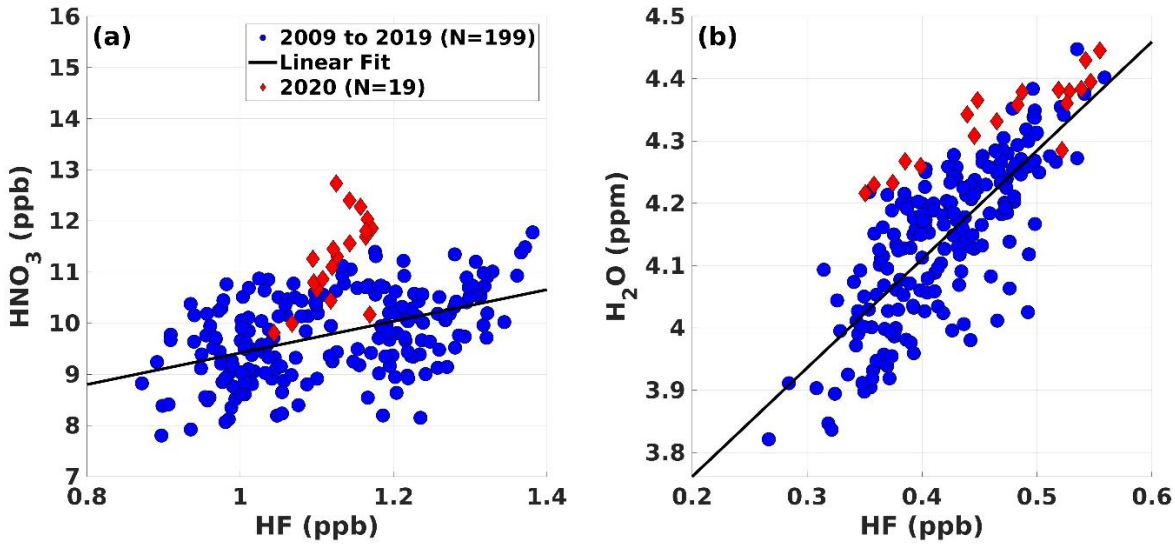

Figure 4: Tracer-trace correlation between ACE-FTS (a) HNO_3 and HF at the altitude of 25 km, and (b) H_2O vs HF at the altitude of 17 km corresponds to latitude range from -60° to -90°. The blue circles correspond to the period March of 2009–2019, the red diamonds to the period March 2020, and the solid black line is a regression line. Here, 'N' is the number of data points used for regression analysis for both subplots.

The Atmospheric Chemistry Experiment - Fourier Transform Spectrometer (ACE-FTS) obtained HF is regressed against HNO_3 and H_2O at altitudes of 25 km and 17 km respectively during March 2009–2019 (Fig. 4). The results suggested that the HNO_3 was produced through a chemical process as the data corresponding to March 2020 (red diamond in Fig. 4a) deviate much from the regression line (black line). In contrast, increased H_2O is transport-related as the data are close to the regression line (Fig. 4b) and likely carried to the lower stratosphere by the smoke plumes from the black summer event (Schwartz et al., 2020). The production of HNO_3 in the lower stratosphere is governed by the heterogeneous chemical reactions in dinitrogen pentoxide (N_2O_5) hydrolysis, which can be written as (Zhang et al., 1995):

$$N_2O_5 + H_2O \rightarrow 2HNO_3 \quad \text{(R1)}$$

To confirm the involvement of the N_2O_5 hydrolysis process, H_2O, N_2O_5, and HNO_3 from ACE-FTS, and k_{ext} at 745 nm from OMPS at 25 km altitude from February to May 2020 are analyzed and shown in Fig. 5. A coinciding depletion in ACE-FTS N_2O_5 at the altitude of 25 km can be observed during the same period (Fig. 5c). Thus, we have performed a similar tracer-tracer correlation analysis for N_2O_5 (Fig. S2). The result indicates that N_2O_5 is chemically depleted in the lower stratosphere, suggesting the possible role of the N_2O_5 hydrolysis process. In general, the stratospheric background aerosols provide a surface for H_2O to condense and gas-phase N_2O_5 reacts with it to form HNO_3.

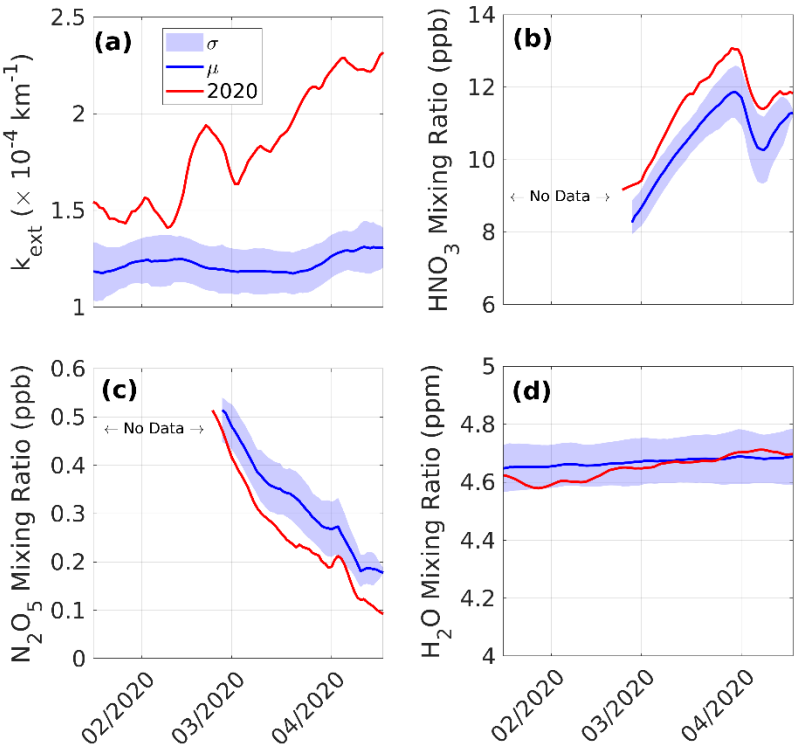

Figure 5: OMPS obtained (a) k_{ext} at 745 nm, and ACE-FTS obtained (b) HNO_3, (c) N_2O_5, and (d) H_2O mixing ratio at the altitude 25 km averaged between the latitude band -60° to -90°. Here, 'σ' represents the standard deviation with respect to the background mean 'μ' estimated for the period 2009–2019. The x-ticks mark the middle of each month.

The background mean of k_{ext} remains ~1.25×10^{-4} km^{-1} between February to May (Fig. 5a). But since early 2020, k_{ext} gradually increased to peak at 2.4×10^{-4} km^{-1} by April 2020. This increasing trend of k_{ext} could be attributed to the coupled effect of the transportation of even more bushfire aerosols from mid to high latitude as days pass and aerosol ages, the bushfire aerosols mixed with stratospheric sulfate aerosols result in an increased size and extinction coefficient (Li et al., 2021; Ohneiser et al., 2022). The simultaneous production and depletion of HNO_3 and N_2O_5 exceeded the respective standard deviations and substantiated that HNO_3 is produced through N_2O_5 hydrolysis (Fig. 5b and c).

During Austral winter, due to the continued lack of solar radiation, the temperature of the polar region decreases to less than 195 K, which results in the condensation of these trace gases on stratospheric aerosols, forming PSC. The near-simultaneous decrease in aerosol loading (as discussed in Sect. 4.2), HNO_3, and H_2O at the lower stratosphere during the early winter of 2020 suggests that these changes possibly affected the PSC formation. A comprehensive investigation of PSC dynamics was carried out using CALIPSO measurements and is discussed in the next section.

4.4. Impact of the black summer event on the PSC during 2020

We first investigated the onset of PSCs during 2020 with respect to the previous years. The onset of each type of PSC is determined for the years 2009 to 2020 (excluding 2015) and provided in a supplementary section (Table S1). The onset is defined as the first instance when each PSC type is detected by CALIPSO. We did not observe an early-onset of any PSCs during 2020. However, the onset of STS occurred on 26th May 2020 which is slightly later than the usual onset period of STS. It should be noted that there are sub-visible PSCs which are not detected by CALIPSO as those PSCs' optical properties are below the CALIPSO detection threshold (Lambert et al., 2012, 2016). Hence, the actual onset could be 1 to 3 days earlier than these dates. The sub-visible PSCs are often studied through depletion in HNO_3 during early winter. We used MLS HNO_3 to check whether there is early/late depletion in HNO_3 leading to early/late onset of PSCs during 2020 at the altitude of 20 km (Fig. S4). Figure S4 shows that the depletion of HNO_3 usually occurs during post-mid of May every year at an altitude of 20 km and the pattern remained unchanged for the year 2020 suggesting no sign of early depletion of HNO_3. This observational evidence from MLS HNO_3 and CALIPSO PSC suggests there is neither early depletion of HNO_3 nor early onset of PSCs.

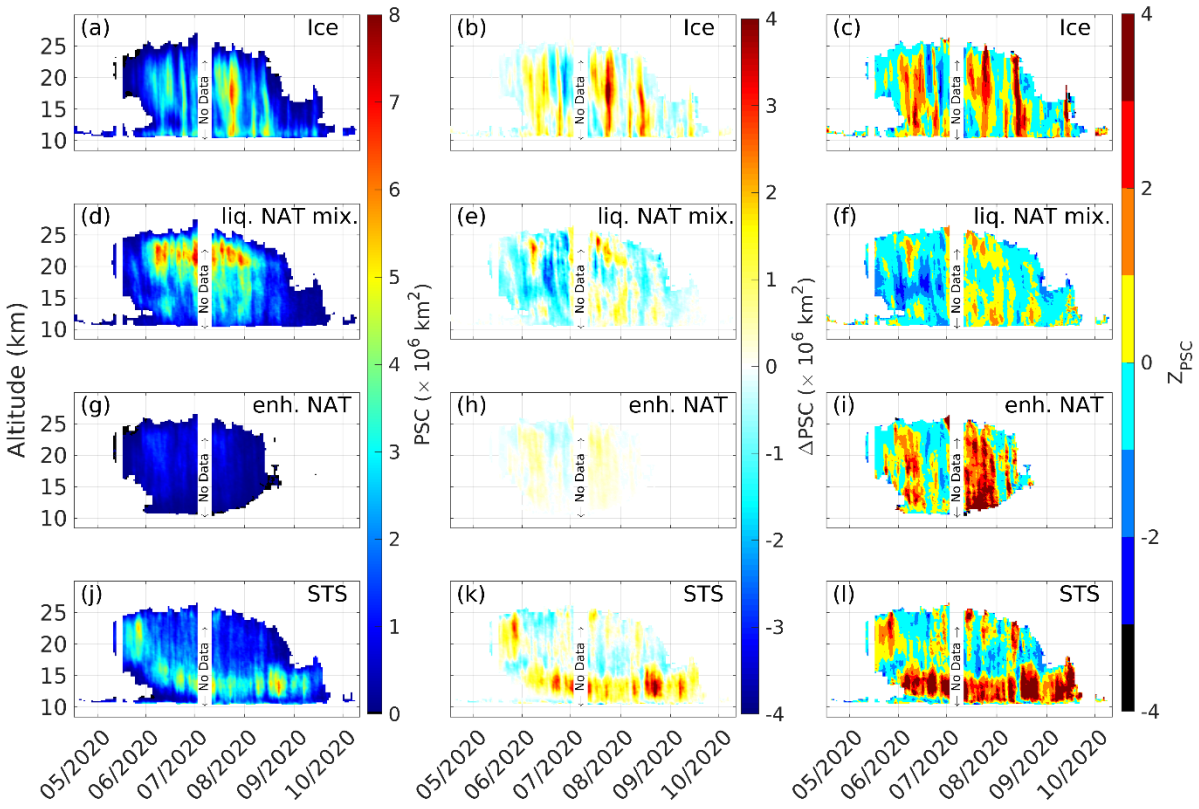

Figure 6: CALIPSO Antarctic PSC areal coverage (left column, panels a, d, g, and j), anomaly (middle column, panels b, e, h, and k), and standardized anomaly (right column, panels c, f, i, and l) for the year 2020. Here, 'liq. NAT mix.' is a liquid-NAT mixture and enh. NAT is enhanced NAT.

The Antarctic PSC areal coverage for each PSC for the year 2020, and corresponding anomalies and standardized anomalies are estimated (as described in the methodology Sect. 3.2) and are shown in Fig. 6. The anomaly in the total PSC areal coverage is shown in Fig. S5. CALIPSO detected the PSC from late May onwards (Fig. 6). Around the same time, depletion in HNO_3 is also observed through MLS (Fig. 3). Peak positive anomaly of up to 4×10^6 km^2 is exhibited by ice at the altitude between 15 km and 20 km during the second week of August 2020. Followed by ice, the Supercooled Ternary Solution (STS) exhibited a high positive anomaly, which peaked up to 3.5×10^6 km^2 at an altitude between 12 km and 15 km during early September 2020 (Carslaw et al., 1994; Molina et al., 1993; Ravishankara and Hanson, 1996). Similarly, an increase in enhanced NAT areal coverage is observed but its contribution to the total PSC areal coverage is negligible. It is evident from Fig. 6 (b, h, and k) that the positive anomalies in the areal coverage of PSCs like ice, STS, and enhanced NAT exceeded three standard deviations with respect to the background mean. Furthermore, during June and July 2020, areal coverage of liquid−NAT mixtures decreased significantly, leading to a negative anomaly of up to 2.5×10^6 km^2, which is more than two standard deviations from the background mean (Fig. 6 (e and f)). During the same period, a significant increase in ice areal coverage of up to 2×10^6 km^2 is observed, exceeding two standard deviations (Fig. 6 (b and c)).

4.4.1 Interannual variabilities of polar vortex and polar stratospheric clouds

In general, the PSC exhibits a strong interannual variation owing to the polar vortex dynamics such as vortex temperature and area. So, the statistics such as minimum, maximum, mean, and standard deviation of the PSC volume for each PSC type observed from 2009 to 2020 along with their relationship with polar vortex dynamics are studied in detail and shown in Fig. 7. Here, the polar vortex is defined as the region enclosed by the 32 PVU (Potential Vorticity Unit) potential vorticity contour, following the definition from (Kondragunta et al., 2005). The vortex area is quantified as the total area within this defined region, while the vortex temperature represents the mean temperature over the same area. The potential vorticity and temperature are taken from the ERA5 operational analysis dataset.

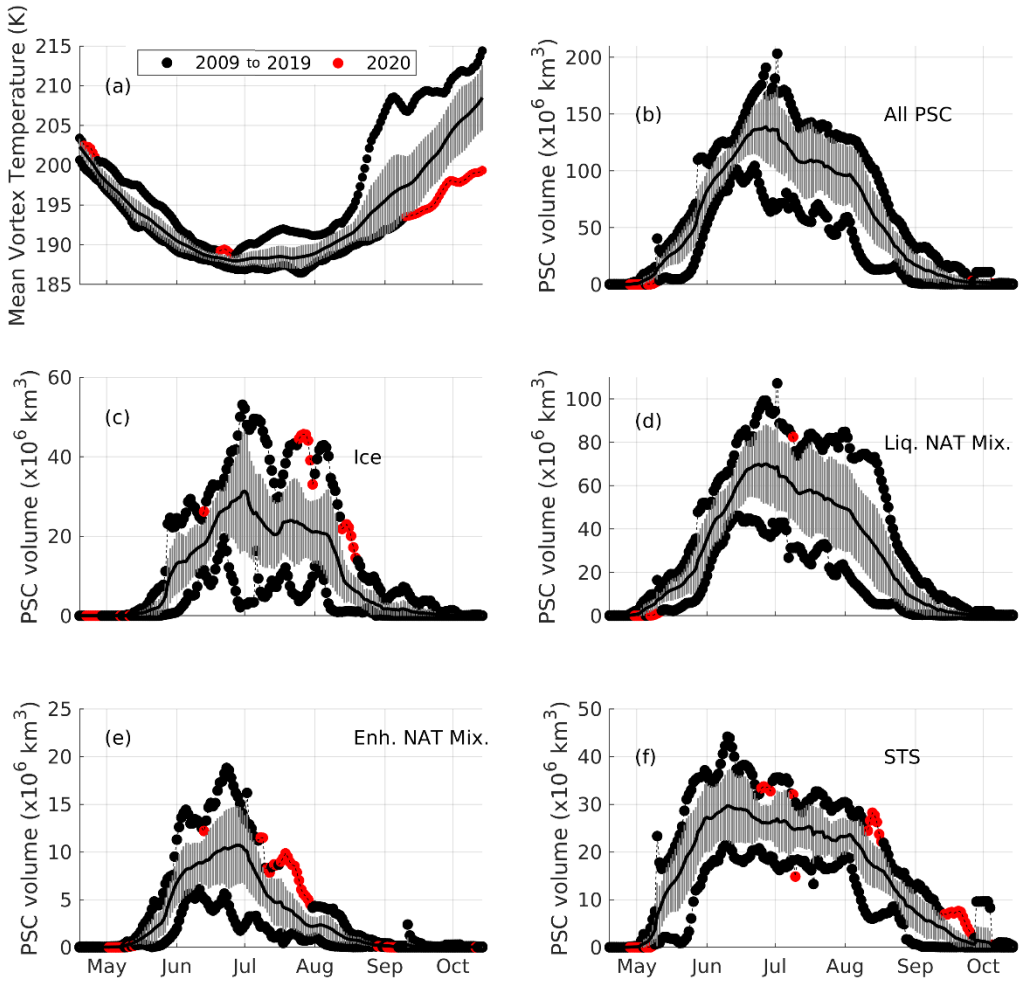

Figure 7: Time series of the CALIPSO obtained PSC volume over the Antarctic from 2009 to 2020 (excluding 2015) are shown. Panel (a) shows the mean vortex temperature obtained from ERA5 operational analysis at the potential temperature of 450 K, and panel (b to f) shows the volume of total PSC, ice. Liq. NAT Mix., Enh. NAT Mix, and STS. The black solid line represents the mean PSC volume, and the vertical lines represent the standard deviation. The daily maximum and minimum PSC volumes are color-coded according to the period in which they occurred. The red-filled circles mark the anomalous high/low value in PSC volume and mean vortex temperature during 2020 and black-filled circles mark the period from 2009 to 2019.

During early May and June 2020, the mean vortex temperature was the highest compared to the background period (from 2009 to 2019, excluding the year 2015) (Fig. 7a). In contrast, the mean vortex temperatures for the remaining months up to September 2020 were neither the warmest nor the coldest. However, after September 2020, the mean vortex temperature dropped to its lowest levels ranging from 194 K to 200 K which can be attributed to the prolonged vortex period and ozone depletion. Owing to this colder environment, the STS PSC continued to appear even after September 2020 and resulted in the highest STS PSC volume with respect to the background period. However, this colder condition is not sufficient enough to affect the formation of other PSC types (i.e., notable positive anomaly) after September 2020 (Fig. 6 and Fig. 7). In terms of total PSC volume (i.e.,

a sum of the volume of total PSC types), there is no anomalous behavior in total PSC volume is observed which is also reported by Li et al., (2024). However, upon investigating the individual PSC volume, we found that ice, enhanced NAT, and STS PSC exhibited anomalously high volume for a certain period during 2020, exceeding one standard deviation (Fig. 6 c, i, and l) as well as the recorded decadal high value (Fig. 7 c, e, and f; marked with red-filled circles). The period 8th to 14th August 2020 and 27th August to 9th September 2020 recorded the highest ice PSC volume among the years from 2009 to 2020, reaching up to 45×10^6 km^3 and 22×10^6 km^3, respectively. Similarly, the year 2020 recorded the highest enhanced NAT PSC volume of up to during 21st July to 30th July 2020. For the STS PSC, the second week of July and the last week of August 2020 recorded the highest PSC volume. However, liquid-NAT mixture PSC volume did not exhibit significant anomalies relative to other PSC types. As the magnitude of PSC volume also depends on the polar vortex dynamics, we investigated the polar vortex area and mean temperature for the year 2020 and compared it with the background period.

Early-May and early-June 2020 are the warmest periods in the background period (Fig. S3 a). But during most of the days from late-June to early-August 2020, the Antarctic polar vortex area is recorded to be the highest, ranging between 23×10^6 km^2 and 32×10^6 km^2. In contrast, this period is not the coldest as revealed by the mean vortex temperature. We checked the role of this increased polar vortex area during 2020 for the increased PSC by investigating the anomaly in vortex occurrence frequency at a potential temperature level of 450 K and PSC volume from June to August 2020. For this purpose, a positive anomaly in vortex occurrence frequency greater than one standard deviation with respect to the background period (the single-hatched region in Fig. 8) and a negative anomaly greater than one standard deviation (the cross-hatched region in Fig. 8) are overlayed on the anomaly in monthly PSC volume.

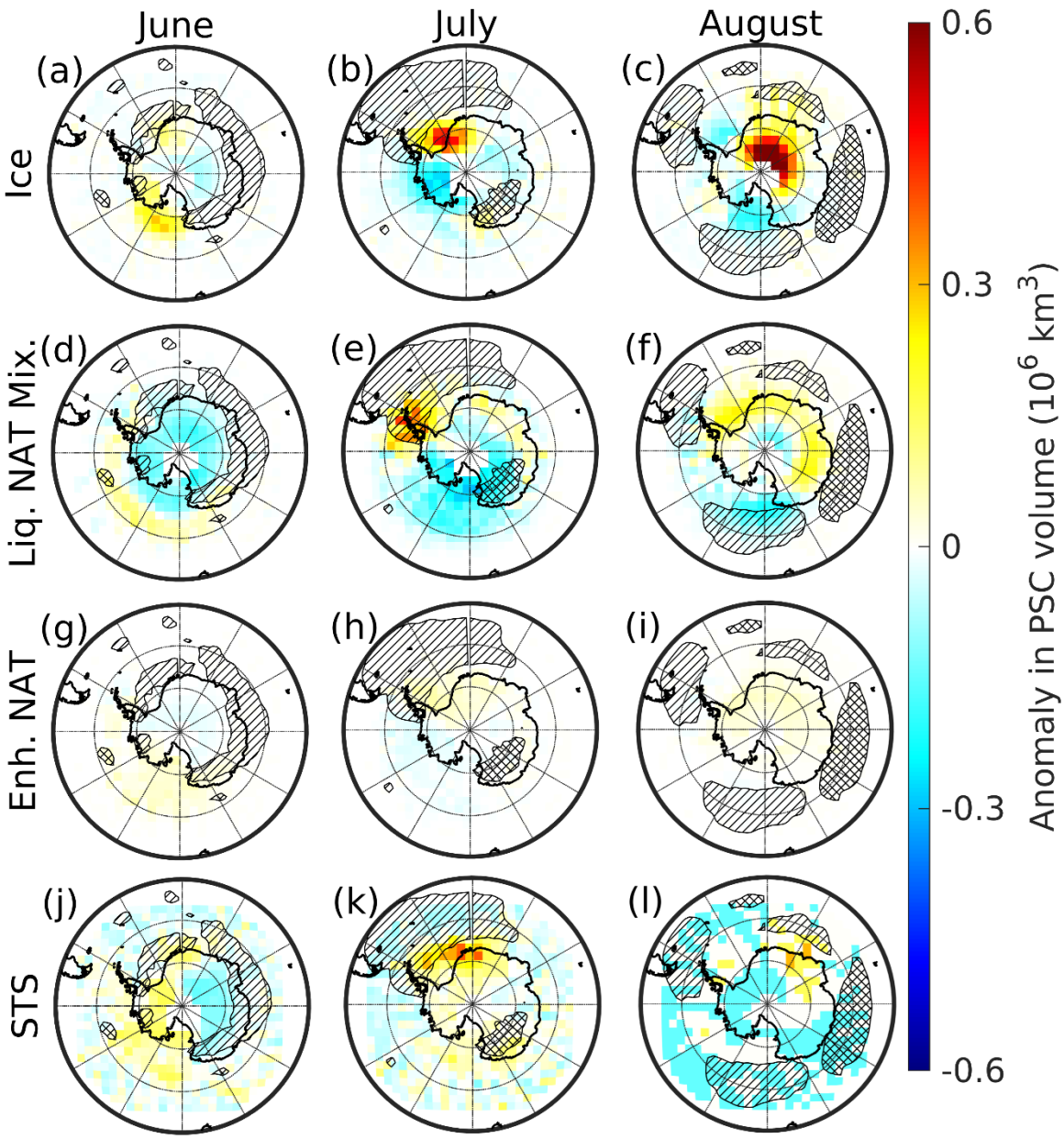

Figure 8: Monthly mean PSC volume anomalies for June (left column), July (middle column), and August (right column) are shown. Single-hatched regions indicate a positive anomaly in polar vortex occurrence frequency exceeding one standard deviation, while cross-hatched regions indicate a negative anomaly exceeding one standard deviation.

During June 2020, the vortex occurrence frequency exceeded one standard deviation over the eastern Antarctic and northeastern regions (marked with single hatching in Fig. 8, panels in the left column), indicating a significant expansion of the polar vortex in these areas. However, no positive anomalies in any PSC types were observed over the same region, suggesting that the increased vortex area during June 2020 did not influence PSC formation (Fig. 8, left column). In July 2020, the polar vortex shifted off the South Pole toward the Antarctic Peninsula, resulting in a significant positive anomaly in vortex occurrence frequency over the northwestern region (marked with single hatching in Fig. 8, middle column) and a negative anomaly over the southeastern region (marked with

cross-hatching in Fig. 8, middle column). Over the Antarctic Peninsula, a positive anomaly in liquid-NAT mixture PSC volume slightly overlapped with this stretched vortex area, while no other PSC types exhibited anomalous behavior (Fig. 8, middle column). By August 2020, the vortex expanded further, stretching toward the Antarctic Peninsula while compressing over the eastern Antarctic region (Fig. 8, right column). Although a significant increase in PSC volume was observed during this month, particularly for ice and liquid-NAT mixtures, these PSCs remained confined close to the South Pole. This again suggests that the increased polar vortex area did not influence PSC formation or contribute to the observed positive anomalies in PSC volume. As discussed earlier in Fig. 7, except liquid-NAT mixture, the volume of other PSCs exhibited anomalous behavior during certain periods of 2020. So, we compared the mean vortex temperature with the ice PSC volume during 8th to 14th August 2020 (Fig. 9 a) and 27th August to 9th September 2020 (Fig. 9 b), enhanced NAT mixture during 21st to 30th July 2020 (Fig. 9 c), and STS during 23rd to 30th August 2020 (Fig. 9 d) with previous years. These periods are chosen as during this period at least one type of PSC recorded its highest volume during 2020 (Fig. 7; marked with red-filled circles). The mean vortex temperature from 8th to 14th August 2020 is ~188 K which is considerably warmer than previous years (such as 2011, 2016, 2017, 2018, and 2019). Despite this relatively warm condition, the mean ice PSC volume is observed to be 46×10^6 km^3 (Fig. 9 a), which is significantly higher than in previous years. Similarly, from 27th August to 9th September, the mean vortex temperature is ~191 K. Once again it is not the coldest period when compared to the years from 2009 to 2019. Yet, the mean ice PSC volume peaked to 22.5×10^6 km^3 which is two-folds higher than the previously recorded values. Similar observations are made in the case of enhanced NAT mixture and STS PSC volume (Fig. 9 c and d) where significant increases in their respective PSC volume are observed despite the vortex temperature comparable to the previous years.

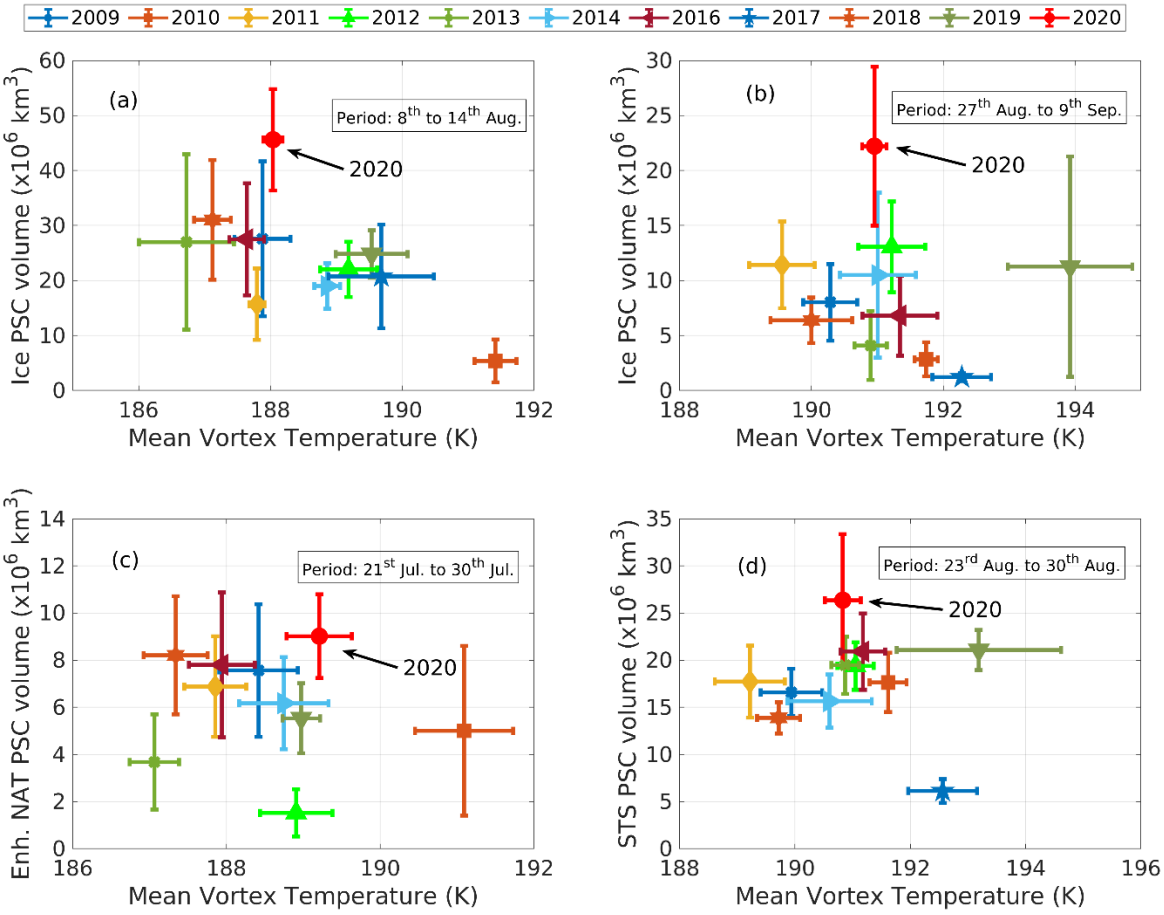

Figure 9: The relationship between mean vortex temperature and ice (panels a and b), enh. NAT (panel c), and STS (panel d) PSC volume are shown. The center of each marker represents the mean value, while the vertical and horizontal lines indicate one standard deviation of daily PSC volume and mean vortex temperature for each period (shown in a rectangle box) respectively. The black arrows in each panel point to the data corresponding to the year 2020.

This analysis indicates that the increased PSC areal coverage and volume cannot be attributed to vortex dynamics, such as variations in vortex area or temperature. Instead, we attribute these anomalously high PSC areal coverage and volumes to the intrusion of bushfire aerosols from the black summer event. In summary, the stratosphere intruded bushfire aerosols result in increased production of HNO_3 through enhanced N_2O_5 hydrolysis process while increasing HNO_3 containing PSCs such as STS, and enhanced NAT mixture. But despite the relatively high availability of HNO_3 during 2020, no significant anomaly is observed in the liquid-NAT mixture. One possible explanation for this observation could be the rapid conversation of NAT particles into ice PSC as NAT can act as nuclei for ice formation. NAT can serve as efficient nuclei for ice formation (Hoyle et al., 2013). To verify this hypothesis, we performed Lagrangian backward trajectory analysis of the ice PSC as well as liquid-NAT mixture PSC to study their respective formation pathways as discussed in the methodology section (Sect. 3.3), and the results are discussed in the next section.

.

4.5. Formation pathways of liquid–NAT mixture and ice PSC

In this section, the formation pathways of ice and liquid-NAT mixture PSCs are presented in the form of case studies. Here we discuss a few case studies which are considered representative of each formation pathway of liquid-NAT mixture and ice PSCs. A total of 5 case studies are discussed: 3 cases for liquid-NAT mixture PSC and 2 cases for ice PSC. The liquid-NAT mixture and ice PSCs are selected according to the selection criteria discussed in Sect 3.3 and backward trajectories are calculated using the CLaMS trajectory module with meteorological parameters obtained from the ERA5 operational analysis dataset. The liquid-NAT mixture can form either through an ice-free nucleation process or an ice–assisted nucleation process. The evidence of the former one is discussed through case no. 1 and the latter one is discussed through case no. 2 to 3 below. Similarly, the evidence of the formation of ice through NAT-assisted formation pathway and NAT-free formation pathway are discussed in case no. 4, and 5, respectively.

4.5.1 Ice-free nucleation of liquid-NAT mixture PSC

In this section, we discuss case no. 1 where 'NC' precedes the liquid-NAT mixture along the trajectory. In this case, there is no evidence of the formation of ice either through CALIPSO observation or conditions conducive for ice formation, suggesting the possibility of ice-free nucleation of liquid-NAT mixture.

Case no. 1: NC precedes liquid-NAT mixture

On 10-07-2020, at 18:00 UTC, CALIPSO detected a liquid-NAT mixture at a latitude of -69.1° and longitude of 99.15°, with a potential temperature of 484 K. This observation is marked by a yellow diamond in Fig. 10 (a) and corresponding CALIPSO scan track is shown as a solid grey line and CALIPSO PSC orbit curtain plot is shown in Fig. S7a. The dashed black line in Fig. 10 (a) represents the calculated 48 h backward trajectory of this PSC, with the color indicating the temperature history of the air parcel in $_{ice}$ coordinates (i.e. ambient temperature - the frost point (T_{ice})). The temperature 'T' is obtained from ERA5 operational analysis, and T_{ice} is estimated using the ERA5 pressure, and mean MLS H_2O mixing ratio found along the trajectory following Marti and Mauersberger, (1993).

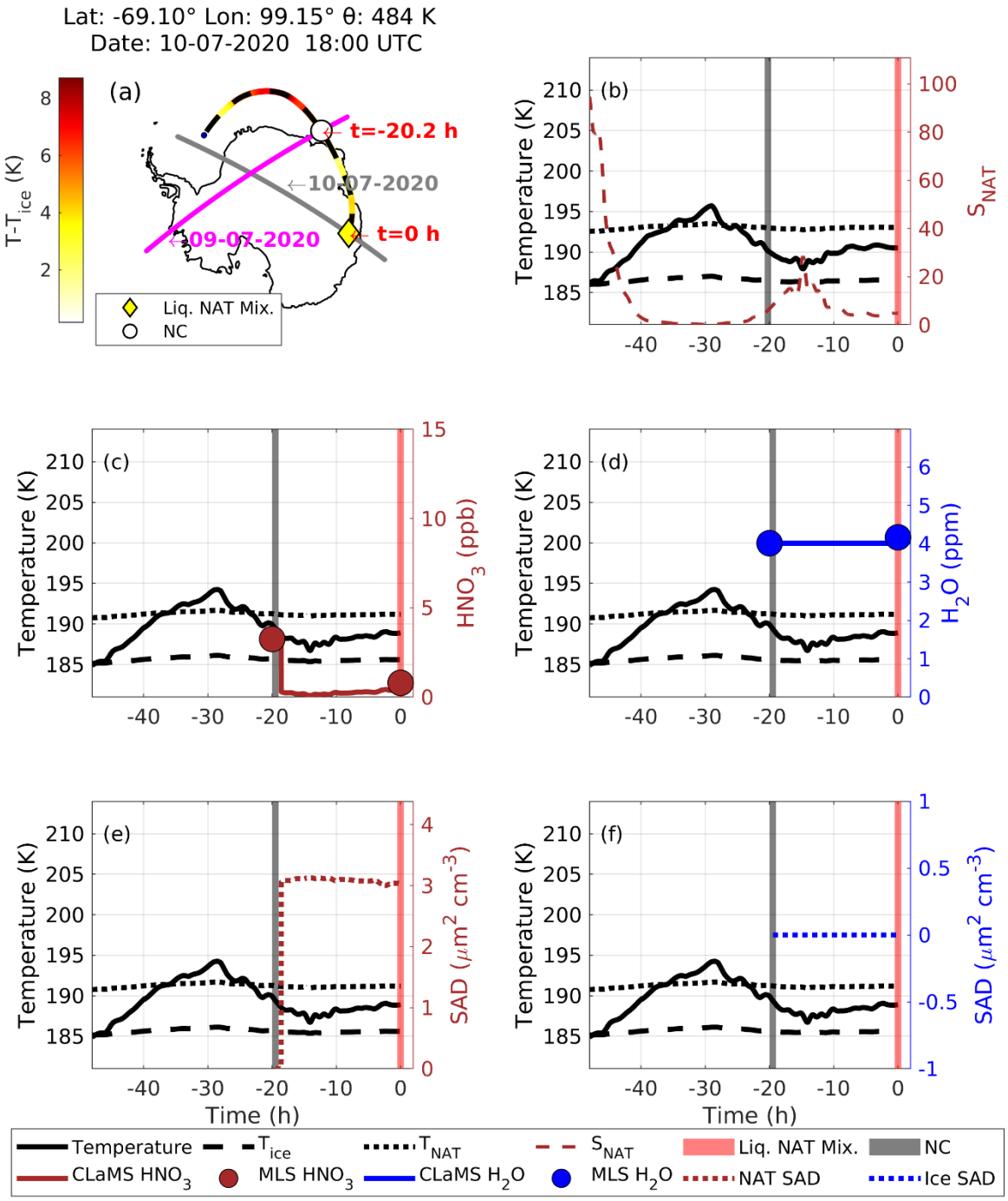

Figure 10. (a) The Lagrangian backward trajectory for a 48 h period starting at time, t = 0 h (corresponding to 18:00 UTC 10-07-2020). Here, the dashed black line is the backward trajectory and the color along this trajectory is the temperature at the T-T_{ice} coordinate. The yellow diamond represents the observed liquid-NAT mixture from the CALIPSO scan track (solid grey line) corresponding to 10-07-2020 and the corresponding CALIPSO PSC orbit curtain plot is shown in Fig. S7b. The complete coordinate of this liquid-NAT mixture is given in the title. The white circle represents the observed 'No Cloud (NC)' at the time, t = -20.2 h from the CALIPSO scan track (solid magenta line) corresponding to 09-07-2020. (b) the saturation ratio over NAT (S_{NAT}) (dashed brown line) and vertical bars mark the liquid-NAT mixture (red) and 'NC' (grey). (c) The brown circle marks the MLS HNO_3,

and the solid brown line represents the CLaMS HNO_3. (d) The blue circle marks the MLS H_2O, and the solid blue line represents the CLaMS H_2O. (e) the NAT surface area density (SAD) (dotted brown line), (f) The ice surface area density (SAD) (dotted blue line).

The backward trajectory revealed that CALIPSO observed 'No Cloud (NC)' along this trajectory 20.2 hours earlier (at the time, t = -20.2 h), on 09-07-2020, marked by a white circle in Fig. 10(a). The temperature history shows that between these two observations, the temperature did not decrease below the T_{ice}, indicating that the condition is not conducive for ice formation. At the time of the NC observation, the temperature was ~189 K which is 2 K below the NAT temperature (T_{NAT}). During this time, MLS observed gas-phase HNO_3 and H_2O mixing ratios are 3.5 ppb and 4 ppm, respectively (Fig. 10 c and d). Using these as initial conditions, a CLaMS box model run was performed from t = -20.2 h to 0 h, simulating the evolution from the NC to the liquid-NAT mixture. After 20.2 hours, the MLS HNO_3 decreased from 3.5 to 0.5 ppb, with no significant change in MLS H_2O. Figure 10 (c) and (d) show that the CLaMS modeled uptake of HNO_3 and H_2O which agrees well with the MLS observations. Furthermore, the CLaMS box model run indicates that the NAT surface area density (SAD) increased to nearly 3 $\mu m^2\ cm^{-3}$ (shown in Fig. 10 (e)), while the ice SAD remained at 0 $\mu m^2\ cm^{-3}$, confirming that no ice formation occurred before the observation of the liquid-NAT mixture. During the transition from 'No Cloud' (NC) to the liquid-NAT mixture, the saturation ratio over NAT stayed well below 30, further supporting the absence of ice involvement in the formation of the liquid-NAT mixture (Fig. 10 (b)) (Luo et al., 2003; Voigt et al., 2005). Since the liquid-NAT mixture represents the mixture of liquid STS and solid NAT, it should be noted that STS PSC should have formed between this transition and specifically before the formation of NAT. From this detailed case study of ice-free nucleation of the liquid-NAT mixture discussed above, it is evident that the temperature of the trajectories has not decreased below T_{ice}, and S_{NAT} has remained below 30 confirming no involvement of ice during liquid-NAT mixture formation. Another example of STS preceding the observation of a liquid-NAT mixture along the backward trajectory is shown in Fig. S8. Even in this case, the condition is not conducive enough to form ice between the observation of STS and liquid-NAT mixture, confirming that the NAT formed without ice. For brevity, the details about this case are not discussed in detail here.

4.5.2 Ice-assisted nucleation of liquid-NAT mixture PSC

Here, two cases are discussed through case no.2 and case no.3. In the former case, the direct CALIPSO observation of ice preceding the liquid-NAT mixture along the trajectory is presented. In the latter case, CALIPSO observed 'NC' preceding the liquid-NAT mixture, but the conducive conditions for ice formation are found before the formation of the liquid-NAT mixture, indicating the possibility of an ice–assisted nucleation process.

Case no. 2: Ice precedes liquid-NAT mixture

In this case, ice has appeared along the backward trajectory before the appearance of the liquid-NAT mixture, indicating nucleation of NAT on the pre-existing ice PSC. On 05-07-2020, at 23:00 UTC, CALIPSO detected a

liquid-NAT mixture (yellow diamond in Fig. 11 (a)) at a latitude of -66.89° and longitude of 25.89°, with a potential temperature of 510 K. The CALIPSO PSC orbit curtain plot for this observation is shown in Fig. S9. Before this, CALIPSO observed ice PSC along this trajectory at time, t = -43 h during 04-07-2020 (blue star in Fig. 11a).

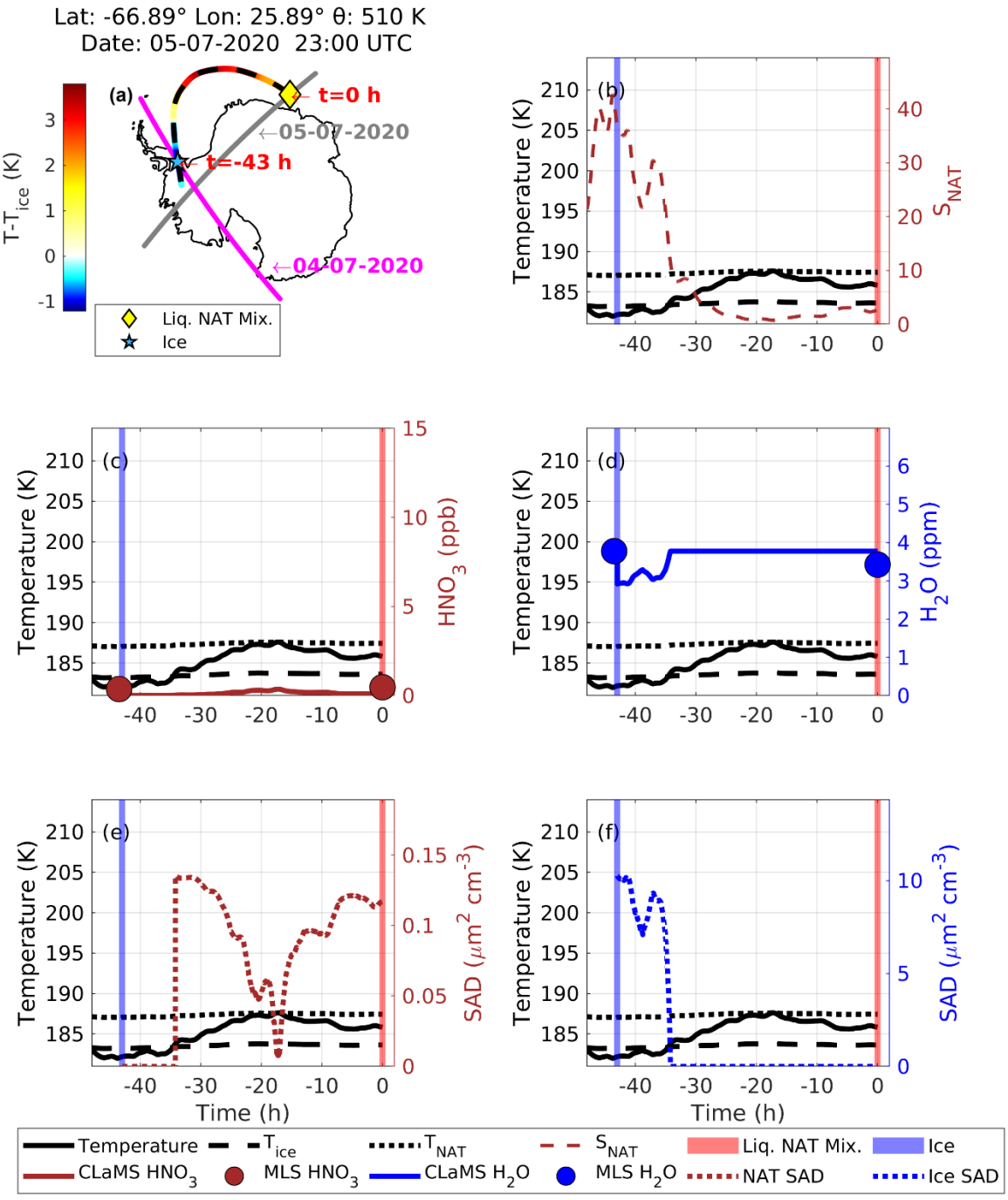

Figure 11. Similar to Fig. 10 but for Case no. 2 where ice preceded the liquid-NAT mixture along the Lagrangian backward trajectory.

At the time of the ice detection, the temperature was approximately 181.5 K, which is 1.5 K below T_{ice}. During this time, MLS observed gas-phase HNO_3 and H_2O mixing ratios are 0.37 ppb and 3.9 ppm, respectively. Furthermore, at this time, according to the CLaMS box model run, ice SAD is ~ 10 $\mu m^2\ cm^{-3}$ and NAT SAD is 0 $\mu m^2\ cm^{-3}$ (Fig. 11 e and f). After this, the temperature gradually increases, exceeding T_{ice} which makes ice SAD to 0 $\mu m^2\ cm^{-3}$, and NAT SAD peaks to 0.14 $\mu m^2\ cm^{-3}$ which is possibly due to nucleation of NAT particles on this ice. During the transition from ice to the liquid-NAT mixture, the maximum S_{NAT} is observed to be 43 at the time, t = -43 h. The MLS observed HNO_3 changed from 0.37 ppb to 0.47 ppb whereas, H_2O decreased from 3.7 ppb to 3.4 ppb. It should be noted that these changes in HNO_3 and H_2O are within MLS measurement uncertainty.

Case no. 3: NC precedes liquid-NAT mixture

In this case, NC is observed before the observation of the liquid-NAT mixture. But along the trajectory, the temperature decreased well below ice formation temperature (i.e., below T_{ice}-1.5 K), indicating the possible formation of ice and thus nucleation of NAT on this ice PSC.

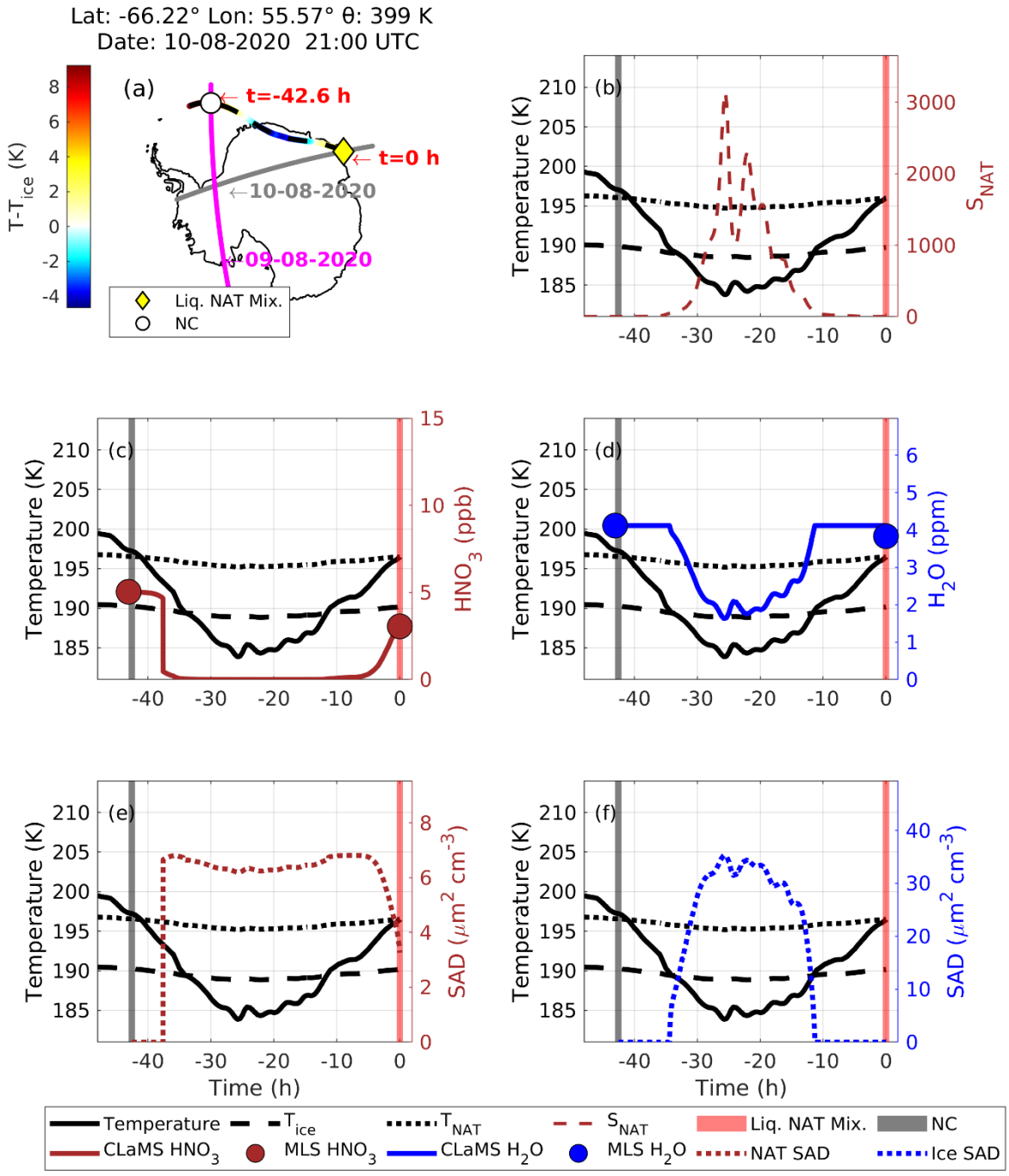

Figure 12. Similar to Fig. 10 but for Case no. 3 where NC preceded the liquid-NAT mixture along the Lagrangian backward trajectory.

On 10-08-2020, at 21:00 UTC, CALIPSO detected a liquid-NAT mixture (indicated by a yellow diamond in Fig. 12 a) at a latitude of -66.22° and longitude of 55.57°, with a potential temperature of 399 K. The CALIPSO PSC orbit curtain plot for this observation is shown in Fig. S10. Before this observation, CALIPSO observed 'No Cloud' (NC) along this trajectory at time t = -42.6 h on 09-08-2020. During that period, the temperature was around 197 K, which is 0.4 K above the T_{NAT}, and MLS measured gas-phase HNO_3 and H_2O mixing ratios of 5 ppb and 4.1 ppm, respectively. These conditions were not favorable for the formation of any type of PSCs. Approximately 4.6

hours later (i.e., at time t = -38 h), the temperature decreased below T_{NAT} by 3 K, which likely promoted the formation of NAT, as supported by the CLaMS box model run, with NAT SAD reaching up to 6 $\mu m^2\ cm^{-3}$ (Fig. 12 e). No ice formation occurred at this stage, as the temperature remained above T_{ice}. The temperature continued to decline, reaching T_{ice} at time t = -35 h, at which point ice began to appear in the CLaMS model, as indicated by the ice SAD (Fig. 12 f).

As the temperature fell to 184 K, which is 5 K below T_{ice}, the ice SAD peaked at 35 $\mu m^2\ cm^{-3}$, suggesting that these ice particles may have nucleated on the previously formed NAT. By this time, the CLaMS model shows that HNO_3 had nearly depleted from the initial 5 ppb to 0.002 ppb, while H_2O decreased from 4.1 ppm to 1.6 ppm. Additionally, S_{NAT} peaked at ~ 3000 (Fig. 12 b). Unlike in cases 1 and 2, where ice was not involved in NAT formation, a significant change in H_2O was observed in this instance due to the formation of ice. Subsequently, the temperature began to increase gradually, reaching above T_{ice} at time t = -11 h, resulting in an ice SAD of 0 $\mu m^2\ cm^{-3}$. At this point, all condensed H_2O evaporated back into the gas phase, returning to the initial level of 4.1 ppm. In contrast, the gas-phase HNO_3 remained below 0.1 ppb. The temperature continued to increase, and at the time, t = 0 h, CALIPSO detected a liquid-NAT mixture, during which MLS observed HNO_3 levels at 3.1 ppb, while the CLaMS modeled HNO_3 is at 3.5 ppb. Throughout this process, MLS HNO_3 decreased from 5 ppb to 3.1 ppb, leaving 1.9 ppb in the condensed phase. In summary, when the temperature was above T_{NAT}, no cloud was observed by CALIPSO. As the temperature decreased below T_{NAT} - 3 K, NAT formed first, followed by ice nucleation when the temperature decreased further below T_{ice}. As the temperature increased, additional NAT particles nucleated on the existing ice. Though the CLaMS box model suggests the presence of ice between t = -35 h to -11 h, there were no co-located CALIPSO observations along the trajectory to verify the presence of ice PSC. However, we identified another backward trajectory related to the CALIPSO-detected liquid-NAT mixture at a potential temperature of 388 K (which is 11 K lower than the current trajectory of 399 K), as shown in Fig. S11. The temperature fluctuations along this trajectory are similar to those in case no. 4, where a co-located CALIPSO observation of ice PSC was recorded at time t = -29.4 h. A similar case, where STS precedes the liquid-NAT mixture, but the temperature along the trajectory decreased below the T_{ice}, creating conditions favorable for ice formation along with the CLaMS box model run, is presented in Fig. S12. Given the similarities between this case and case no. 3, which has been described above, we have not provided a detailed analysis of the case where STS precedes the liquid-NAT mixture.

In these two cases of ice–assisted nucleation process of liquid-NAT mixture, the temperature decreased below $T_{ice,}$ and S_{NAT} increased more than 30. Therefore, the extent to which the temperature decreased below T_{ice} and the extent to which the S_{NAT} increased along the trajectories from the instant of observation of NC/STS/ice to the instant of observation of the liquid-NAT mixture can act as proxies to determine whether the liquid-NAT mixture is formed via ice–assisted or ice-free nucleation process.

4.5.3 Validation of uptakes of HNO_3 and H_2O observed during liquid-NAT mixture formation

During the formation of the liquid-NAT mixture, changes in the gas phase concentrations of MLS HNO_3 and H_2O were observed, as previously discussed. We used the CLaMS microphysical box model to simulate the formation of the liquid-NAT mixture based on the backward trajectories and modeled the uptakes of HNO_3 and H_2O. These

results were validated against the observed uptakes from MLS, as shown in Fig. 13. This result includes both the ice–assisted and ice-free nucleation of the liquid-NAT mixture.

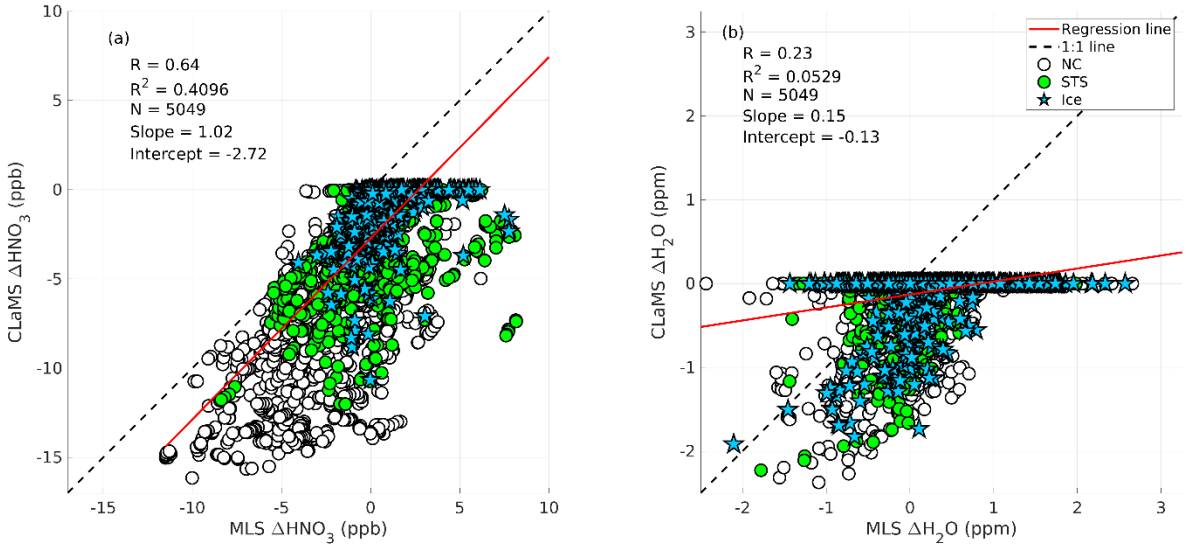

Figure 13. (a) shows a scatter plot of MLS observed change (Δ) in HNO_3 (ppb) against the CLaMS modeled change in HNO_3 (ppb), (b) shows a scatter plot of MLS observed change (Δ) in H_2O (ppm) against the CLaMS modeled change in H_2O (ppm). The dashed line represents a 1:1 fit, and the solid red line represents the linear regression line. Here, 'R' is the correlation coefficient, 'R^2' is the correlation of determination, and N is the total number of data points used. Each marker corresponds to each PSC type preceding to liquid-NAT mixture along the backward trajectory. White-filled circle for NC, green-filled circle for STS, and blue-filled pentagram for ice.

A strong correlation is found between the MLS observed change in HNO_3 (ΔHNO_3) and the CLaMS modeled change in HNO_3, with a correlation coefficient (R) of 0.64 and a coefficient of determination (R^2) of 0.4096 (Fig. 13 a). The intercept of -2.72 suggests that the CLaMS model overestimates the HNO_3 condensation during NAT formation. It could be due to possible cold bias in temperature from ERA5 operational analysis which is used in this study. Due to this cold bias, the CLaMS model overestimates the condensation of HNO_3, leading to the negative value of intercept. Furthermore, significant HNO_3 uptake of up to 12 ppb, as observed by MLS, occurs when NC preceded the observation of the liquid-NAT mixture along the trajectory (indicated by the grey circle in Fig. 13 a). However, a relatively low HNO_3 uptake is observed for cases where STS preceded the liquid-NAT mixture (marked by the green circle in Fig. 13 a). It is important to note that ice may have formed during the transition from NC/STS to the liquid-NAT mixture, as discussed in case no. 3. Furthermore, in most cases where ice preceded the liquid-NAT mixture along the trajectory, a positive change in MLS ΔHNO_3 is observed and more detailed studies are required to understand these scenarios further.

In the case of H_2O uptake, a weak correlation is found between MLS ΔH_2O and CLaMS ΔH_2O, with a correlation coefficient (R) of 0.23 and a coefficient of determination (R^2) of 0.0529 (Fig. 13 b). In addition to the cold temperature bias in ERA5 operational analysis, this low correlation is also attributed to the fact that in the CLaMS model, the initialized H_2O at the beginning of the trajectory changes only if ice forms during the liquid-NAT mixture formation, resulting in most of the CLaMS ΔH_2O values remaining at zero. However, there are a few instances where changes in H_2O are observed in both CLaMS and MLS, potentially indicating ice–assisted formation of the liquid-NAT mixture. Furthermore, in the CLaMS box model run, for simplicity, other chemical reactions (e.g., N_2O_5 hydrolysis, HCl null cycles) which involve the H_2O are not considered as discussed in methodology Sect. 3.4. Hence, even if such reactions occur and deplete/produce H_2O in a real atmosphere, the CLaMS box model run does not account for them. This simplified box model run likely contributes to the weak correlation between H_2O values from CLaMS and MLS observations. A similar reasoning could apply to HNO_3; however, since the HNO_3 depletion is primarily driven by the NAT formation, the omission of other chemical reactions in the simplified box model does not significantly affect the correlation between HNO_3 values from CLaMS and MLS.4.5.4 Relative percentage contribution of liquid-NAT mixture formation pathway

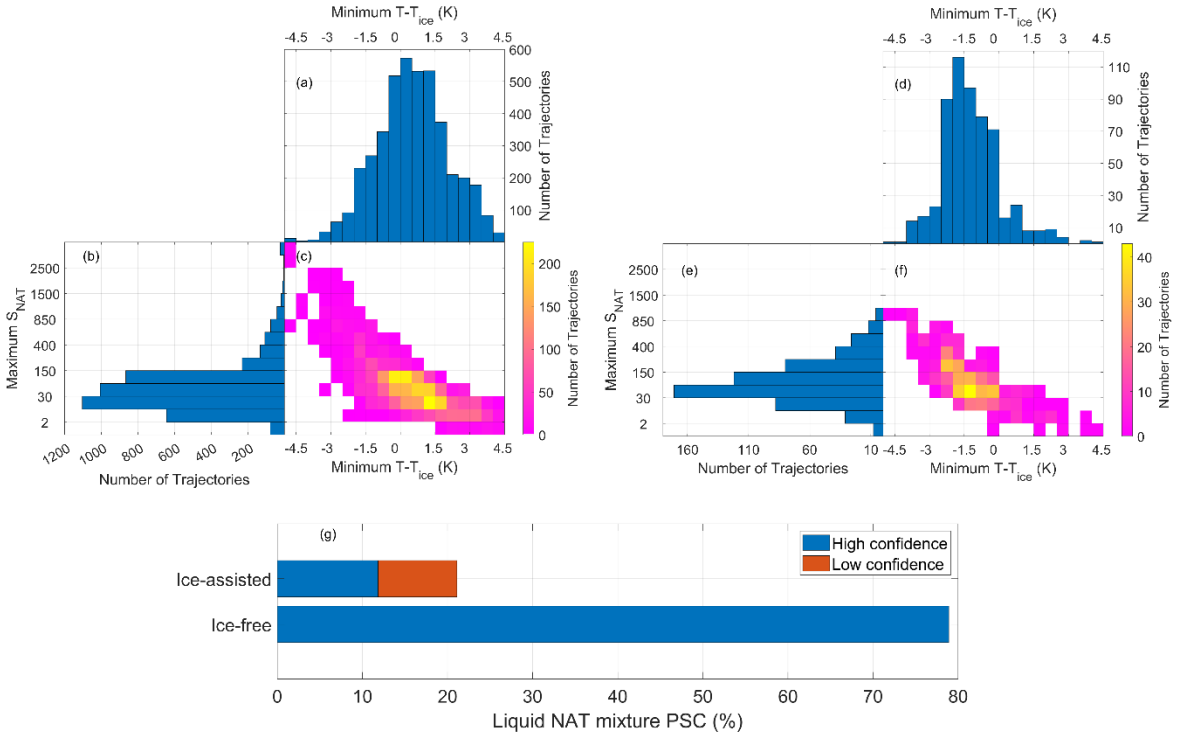

Figure. 14. Histograms and joint histograms of the minimum T - T_{ice} and the maximum S_{NAT} (saturation ratio over NAT) along the trajectories are shown. Panels (a to c) correspond to the backward trajectories where NC/STS preceded the liquid-NAT mixture CALIPSO observation. Panels (d to f) are similar to (a to c) but for the case of ice preceding liquid-NAT mixture. Panel (g) shows the percentage of liquid NAT mixture formed through ice–assisted and ice-free nucleation processes.

As discussed in case studies 1 and 2, the presence of NC/STS preceding the liquid-NAT mixture along the trajectories does not exclude the involvement of ice in the formation of the liquid-NAT mixture. It is possible that

ice could have formed before the observation of the liquid-NAT mixture if the temperature decreased below T_{ice} and reached a state of high NAT supersaturation. Therefore, the extent of temperature decreases below T_{ice} and the corresponding increase in S_{NAT} along the trajectories, from the time of NC/STS observation to the formation of the liquid-NAT mixture, can serve as indicators for whether the liquid-NAT mixture formed through ice–assisted or ice-free nucleation. To investigate this, we created two sets of histograms. Figure. 14 (a to c) shows the histograms of minimum T-T_{ice} and maximum S_{NAT} along the trajectories for cases where NC/STS preceded the liquid-NAT mixture. Figure 14 (d to f) shows similar histograms for cases where ice preceded the liquid-NAT mixture. In all cases, the minimum T-T_{ice} and maximum S_{NAT} were considered only from the time of NC/STS (for Fig. 14 (a to c)) or ice (for Fig. 14 (d to f)) observation until the liquid-NAT mixture formed.

For cases where NC/STS preceded the liquid-NAT mixture, the histogram of minimum T-T_{ice} (Fig. 14 a) shows that most trajectories experienced T-T_{ice} values between -0.5 K and 1.5 K, with the highest peak between 0 and 0.5 K. Similarly, the histogram of maximum S_{NAT} (Fig. 14 b) shows that most trajectories had S_{NAT} values ranging from 15 to 150, with a peak between 15 and 30. A cluster of trajectories (represented by yellow to orange grids) is visible in the joint histogram (Fig. 14 c) within this range. For the formation of ice along these trajectories, the temperature should have reached at least -1.5 K for heterogeneous nucleation of ice, and a high S_{NAT} of > 500 (Luo et al., 2003) should have occurred for nucleation of NAT on these ice particles. Since neither of these is observed and conditions are not conducive to ice formation, it is highly likely that the liquid-NAT mixture formed through an ice-free nucleation process. Case no. 1 which was discussed earlier belong to this category. In addition, when the minimum T-T_{ice} decreased below -1.5 K, the air parcels reached high supersaturation, with S_{NAT} values exceedingly even 500. Case no. 3 which was discussed earlier belongs to this category. Under these conditions, the formation of ice and subsequent nucleation of NAT on this ice is likely, indicating that the liquid-NAT mixture may have formed through ice–assisted nucleation. This observation aligns with previous findings by Luo et al., (2003) on NAT formation over ice under high supersaturation conditions.

For cases where ice preceded the liquid-NAT mixture along the trajectory, the histogram of minimum T-T_{ice} (Fig. 14 d) shows that most trajectories experienced T-T_{ice} values between -2 K and -1 K, with the highest peak between -2 K and -1.5 K. Similarly, the histogram of maximum S_{NAT} (Fig. 14 e) shows that most trajectories had S_{NAT} values ranging from 15 to 150, but for this case, the highest peak occurs between 30-70 instead of 15-30 in previous case. A cluster of trajectories (represented by yellow to orange grids) is visible in the joint histogram (Fig. 14 f) within this range. Case no. 2 which was discussed earlier belongs to this category where ice preceded the liquid-NAT mixture.

From these two sets of histograms, an apparent shift in minimum T-T_{ice} is evident between cases where NC/STS preceded the liquid-NAT mixture (peak between 0 and 0.5 K) and cases where ice preceded the liquid-NAT mixture (peak between -2 and -1.5 K). In contrast, only a subtle shift is observed in maximum S_{NAT}. Therefore, to determine whether ice was involved in the formation of the liquid-NAT mixture, we primarily rely on the minimum T-T_{ice} reached by each trajectory, rather than the maximum S_{NAT}.

For the cases where ice preceded liquid-NAT mixture, we classified these as ice–assisted nucleation of liquid-NAT mixture with high confidence. This is classified with ‘high confidence’, because we have CALIPSO

observation of the presence of ice along the trajectory similar to case no. 2. And, for the cases where NC/STS preceded the liquid-NAT mixture if the temperature along the trajectories decreased less than -1.5 K, we included it to the ice–assisted nucleation of liquid-NAT mixture with low confidence. These are classified with low confidence because ice formation is not directly observed by CALIPSO but possibly formed as the temperature decreased 1.5 K below T_{ice}. For the cases where NC/STS preceded the liquid-NAT mixture if the temperature along the trajectories has not decreased less than -1.5 K, we classified them as ice-free nucleation of liquid-NAT mixture with high confidence. The final retrieved relative percentage of the liquid-NAT mixture formation pathway is shown in Fig. 14 g. It shows that 79 % of the liquid-NAT mixture (corresponding to 2996 backward trajectories) is formed through an ice-free formation process with high confidence. Almost 12 % and 9 % of the liquid-NAT mixture (corresponding to 796 backward trajectories) formed through an ice–assisted formation process with high and low confidence respectively.

4.5.6 NAT-assisted ice formation

In the case of the NAT-assisted ice formation pathway, evidence of a direct CALIPSO observation of liquid-NAT mixture along the backward trajectory ice PSC is given in Fig. S13. For brevity, this case is not discussed in detail here. Instead, another example of NAT-assisted ice formation pathways in which 'NC' precedes ice PSC is elaborated in detail through case no. 4.

Case 4: NC precedes ice PSC

In this case, NC is observed before the observation of ice. On 19-06-2020, at 18:00 UTC, CALIPSO detected ice (blue star symbol in Fig. 15 a) at a latitude of -80.96° and longitude of 6.00°, at a potential temperature of 451 K. Before this, CALIPSO observed NC along this trajectory at the time, t = -37.6 h during 18-06-2020. The CALIPSO PSC orbit curtain plots for these observations are shown in Fig. S14. During the observation of NC, the temperature was around 192.5 K, which is 1 K above T_{NAT} (Fig. 15 b), and MLS measured gas-phase HNO_3 and H_2O mixing ratios of 2 ppb and 3.7 ppm, respectively (Fig. 15 (c and d)). As the temperature is above T_{NAT}, there is no possibility of the formation of PSCs at this time. Approximately 14.6 hours later (i.e., at time t = - 13 h), a strong depletion in CLaMS HNO_3 is observed with CLaMS H_2O mixing ratio unchanged as the temperature decreased below T_{NAT}. By the same time, NAT SAD has increased to ~2.7 $\mu m^2\ cm^{-3}$ (Fig. 15 e). At the time, t = -18 h, ice SAD started increasing gradually as the temperature reached T_{ice} (Fig. 15 f) and reached a peak value of ~20 $\mu m^2\ cm^{-3}$. This suggests the nucleation of ice on the NAT particles.

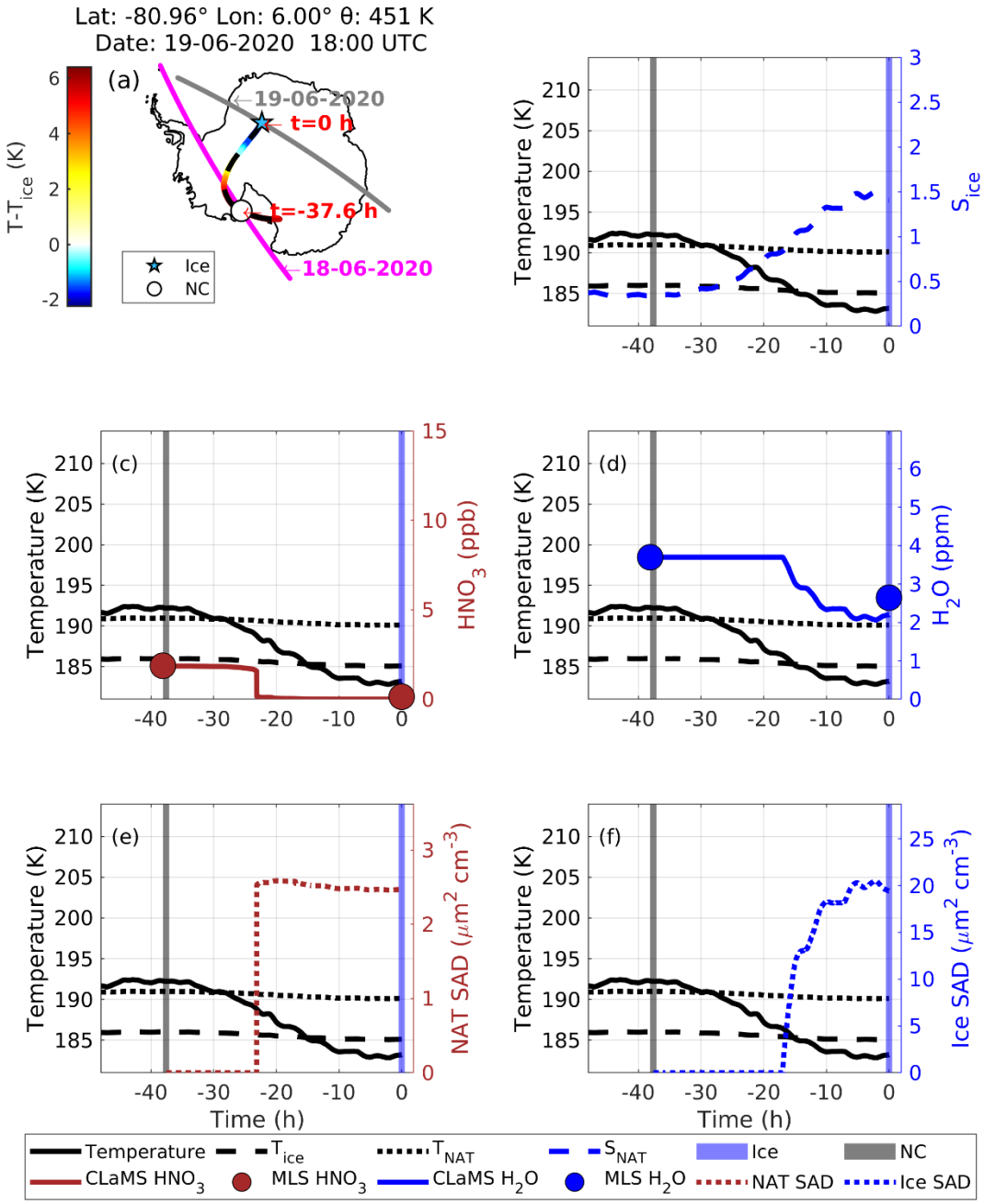
Lat: -80.96° Lon: 6.00° θ: 451 K
Date: 19-06-2020 18:00 UTC
(a)
T-T$_{ice}$ (K)
19-06-2020
t=0 h
t=-37.6 h
18-06-2020
Ice
NC
Temperature (K)
S$_{ice}$
(c)
HNO$_3$ (ppb)
(d)
H$_2$O (ppm)
(e)
NAT SAD (μm^2 cm^{-3})
(f)
Ice SAD (μm^2 cm^{-3})
Time (h)
Temperature
T$_{ice}$
T$_{NAT}$
S$_{NAT}$
Ice
NC
CLaMS HNO$_3$
MLS HNO$_3$
CLaMS H$_2$O
MLS H$_2$O
NAT SAD
Ice SAD

Figure 15. Same as Fig. 10 but for case no. 4 where ice nucleation on NAT is shown.

4.5.7 NAT-free ice formation

In this section, we discuss case no. 5 where the NAT-free ice nucleation process leads to ice formation.

Case 5: NC precedes ice PSC

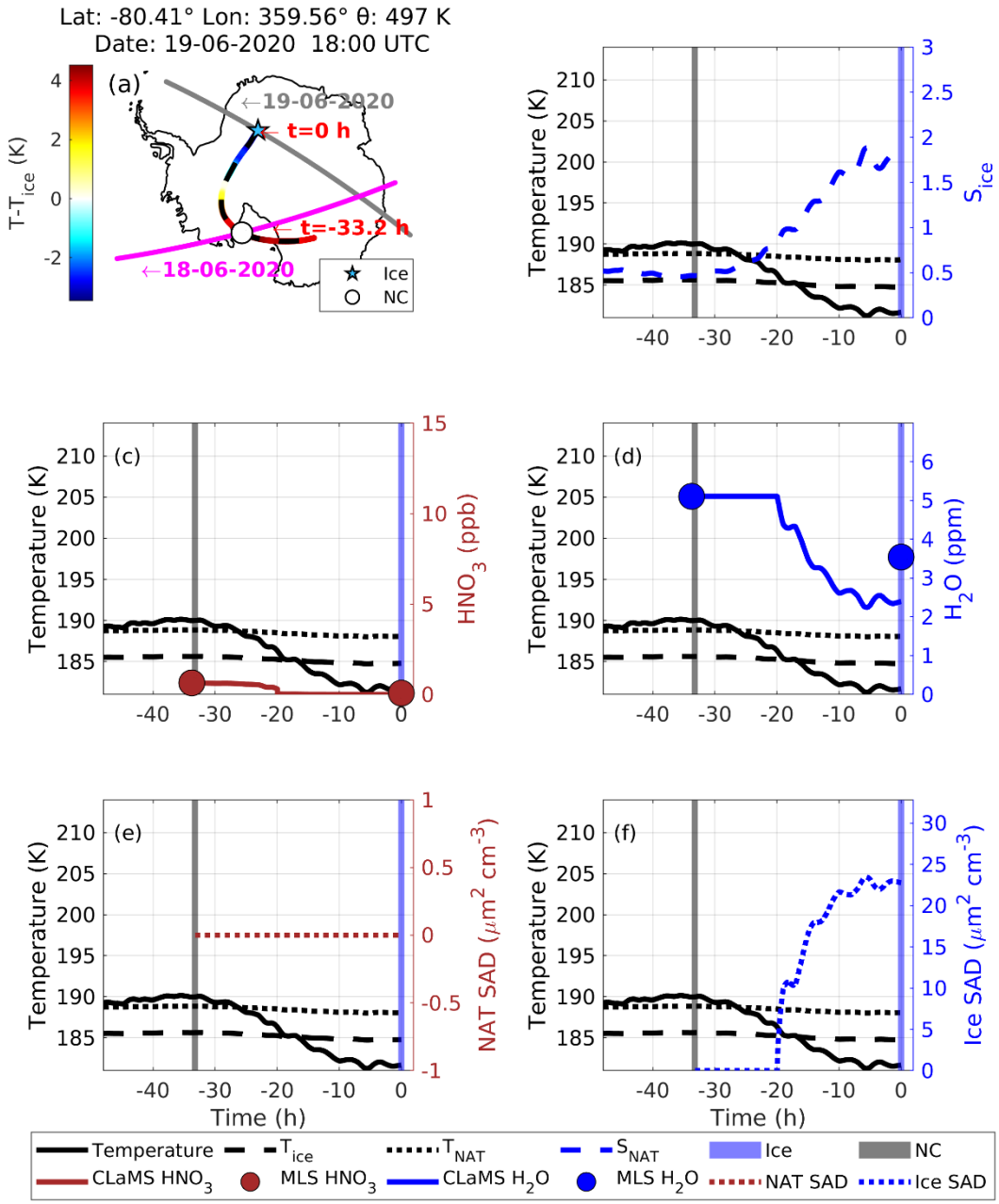

Figure 16. Same as Fig. 10 but for case no. 5 where ice nucleated without NAT.

In this case, NC is observed before the observation of ice along its backward trajectory. On 19-06-2020, at 18:00 UTC, CALIPSO detected ice (blue star symbol in Fig. 16 a) at a latitude of -80.41° and longitude of 359.56°, at a potential temperature of 497 K. Before this, CALIPSO observed NC along this trajectory at the time, t = -37.6 h during 18-06-2020. The CALIPSO PSC orbit curtain plots for these observations are shown in Fig. S15. There are notable similarities between case no. 4 and case no. 5. In both cases, the latitude, longitude, and temperature histories of the observed ice PSC and the preceding NC along the backward trajectory are almost identical. However, the ice PSC in case no. 5 is located at a potential temperature of 497 K (Fig. 17 a), whereas for case no. 4, it is at a relatively lower potential temperature of 451 K (Fig. 16 a). Despite having similar temperature histories, ice formed by nucleating on NAT in case no. 4, while in case no. 5, ice formed without NAT. A key difference between the two cases is the availability of gas-phase HNO_3. For case no. 5, the MLS HNO_3 mixing ratio at the CALIPSO NC observation is 0.6 ppb (denitrified scenario), which is 1.4 ppb lower than that of case no. 4. Hence, compared to case no. 4, for case no. 5 relatively low MLS HNO_3 is observed when the temperature was above T_{NAT}. The CLaMS box model for case no. 5 shows no NAT formation along the trajectory, with NAT SAD remaining at 0 $\mu m^2\ cm^{-3}$ (Fig. 16 e), while for case no. 4, NAT SAD increases to 2.7 $\mu m^2\ cm^{-3}$ (Fig. 16 e). This is because, in case no. 5, there is not enough gas-phase HNO_3 (with just 0.6 ppb) to form NAT as it might have already been removed through the growth of NAT to large size, leading to denitrification before the observation of NC itself. In both cases, ice forms as the temperature drops below T_{ice}, with ice SAD reaching ~23 $\mu m^2\ cm^{-3}$ in case no. 5 which is 3 $\mu m^2\ cm^{-3}$ higher than in case no. 4 (Fig. 16 f). Furthermore, during ice formation, the maximum S_{ice} is ~1.5 in case no. 4, compared to a high supersaturation S_{ice} of 1.8 in case no. 5 (Fig. 16 b). Since ice can form through a homogeneous nucleation process at $S_{ice} > 1.5$, the temperature needs to be 3 K below T_{ice}. But for this case, the temperature is just 2 K below T_{ice}, suggesting heterogeneous nucleation of ice but without NAT. One possibility could be that STS with the inclusion of foreign nuclei could have served as the formation of ice in this case. Another example of STS preceding ice PSC, but liquid-NAT mixture was not formed as modeled by CLaMS is given in Fig. S16. As the bushfire aerosols entered the lower stratosphere at the high-latitude region as shown in Fig. 1 and Fig. 2, it is highly likely that bushfire aerosols also included in the STS along with foreign nuclei. In short, under the denitrified scenario where there is not enough availability of gas-phase HNO_3, ice can form through the NAT-free nucleation process. Based on PSC measurement of lidar on board the HALO (High Altitude and Long Range Research Aircraft), Voigt et al., (2018) observed ice PSCs with a bimodal distribution of particle depolarization ratio on 22 January 2016 over the Arctic region. In which, Lagrangian backward trajectory analysis revealed that the ice with a high depolarization ratio is preceded by NAT from CALIPSO measurement. Furthermore, ice with a low depolarization ratio is preceded by STS. Hence, to investigate the ice formation through NAT-free and NAT-assisted nucleation process cases, we analyzed the depolarization ratio of ice and discussed it in the next section.

4.5.8 Bimodal distribution of depolarization ratio of ice PSC

The depolarization ratio of ice preceded by a liquid-NAT mixture and STS along the backward trajectories are analyzed, with the corresponding probability densities shown in Fig. 17. As discussed through the case studies, after the CALIPSO observation of STS, it is possible that a liquid-NAT mixture formed as temperature decreases and these NAT acted as nuclei for ice formation. Therefore, the probability density of the depolarization ratio for the STS case may reflect not only the formation of ice on STS but also ice nucleated on NAT. The probability

density of the depolarization ratio for ice preceded by a liquid-NAT mixture (solid red line in Fig. 17(a)) peak at 0.35. In contrast, the probability density for ice preceded by STS (solid black line in Fig. 17(a)) shows a bimodal distribution, with a high depolarization mode peaking at 0.26 and a low depolarization mode peaking at 0.07. This observation of the bimodal distribution of depolarization ratio is similar to the findings reported by Voigt et al., (2018). This bimodal distribution suggests that under certain conditions, ice nucleates on NAT/STS, contributing to the mixed depolarization signal. Through the example in Fig. S16 and case no. 5, it is shown that under denitrified conditions, the ice can form through a NAT-free formation pathway.

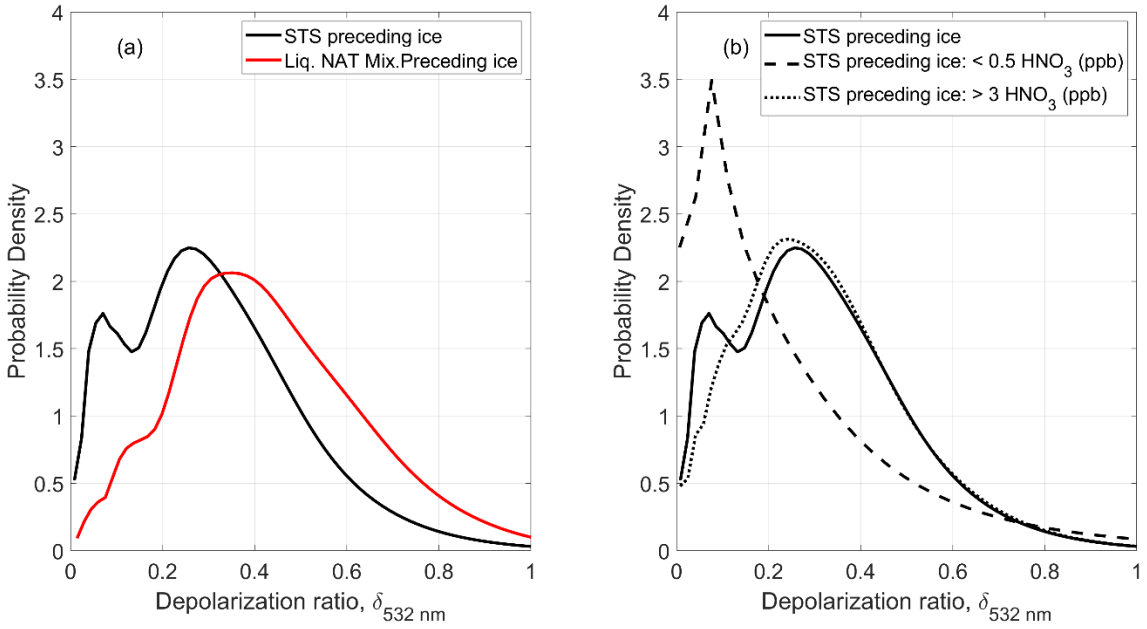

Figure 17. (a) The probability density of the depolarization ratio of ice preceded by STS (solid black line) and liquid-NAT mixture (solid red line) are shown. (b) decomposition of ice preceded by STS cases based on MLS HNO_3 mixing ratios: < 0.5 ppb (dashed line) and > 3 ppb (dotted line).

So, we chose ice PSCs which are preceded by STS under the denitrified condition of MLS HNO_3 < 0.5 ppb (i.e. during the observation of STS along the backward trajectory of ice, the MLS HNO_3 should be < 0.5 ppb), and under normal condition of MLS HNO_3 > 3.0 ppb. Figure 17 (b) shows the depolarization ratio of ice preceded by STS, distinguishing between cases under a denitrified scenario (MLS HNO_3 < 0.5 ppb, black dashed line), and under normal conditions (MLS HNO_3 > 3 ppb, black dotted line). These threshold values of 0.5 ppb and 3 ppb are chosen because they effectively separate the bimodal distribution into two clearly distinguishable modes. The lower threshold (0.5 ppb) captures the conditions where denitrification is significant, and NAT is less likely to form, leading to ice nucleation directly on STS with foreign nuclei inclusion. On the other hand, the higher threshold (3 ppb) represents conditions where sufficient HNO_3 is available for NAT formation, supporting ice nucleation via NAT-assisted processes. These thresholds help differentiate the distinct nucleation pathways reflected in the depolarization ratio distributions. The low HNO_3 case shows a more pronounced peak at lower depolarization values (~0.076), while the high HNO_3 case follows a distribution more similar to the overall STS case with a higher depolarization peak near 0.26. This suggests a potential influence of the availability of gas-phase HNO_3 on the ice nucleation processes. Under normal gas-phase HNO_3 available conditions, ice tends to

form through NAT-assisted nucleation process, and under the denitrified condition where there is not enough HNO_3 to form NAT, ice can form through NAT-free nucleation process i.e., nucleating on STS with foreign nuclei inclusion.

4.5.9 Validation of HNO_3 and H_2O uptakes during ice formation

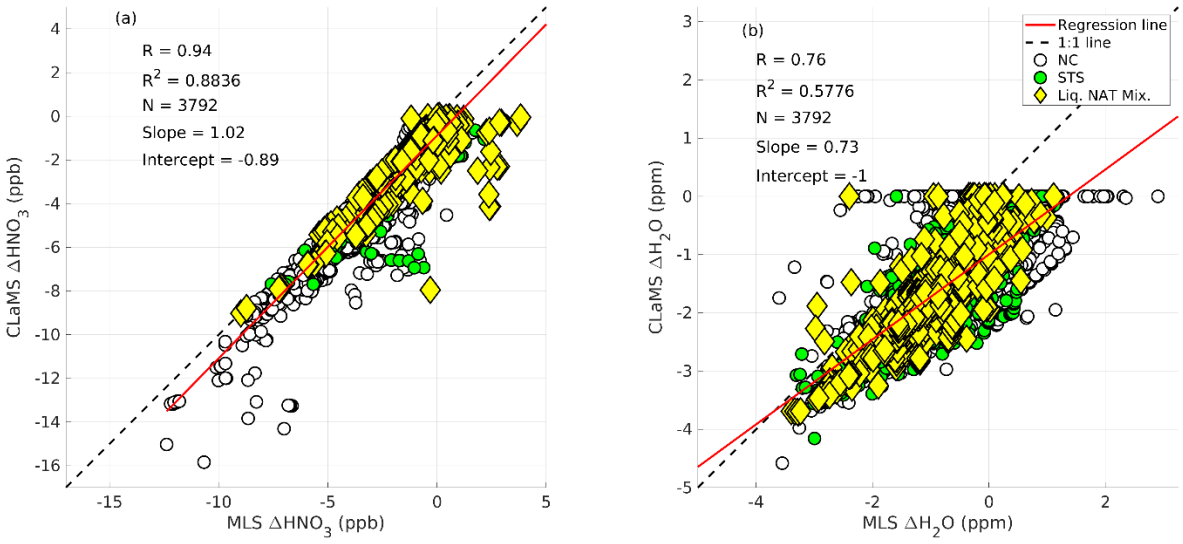

Figure. 18. Same as Fig. 13. But for the case of ice formation.

A strong correlation is found between the MLS observed change in HNO_3 (ΔHNO_3) and the CLaMS modeled change in HNO_3, with a correlation coefficient (R) of 0.94 and a coefficient of determination (R^2) of 0.8836 (Fig. 18a). Similar to HNO_3 uptakes during the formation of liquid-NAT mixture from NC, significant HNO_3 uptake of up to 12 ppb, as observed by MLS, occurs when NC preceded the observation of the ice along the trajectory (indicated by the grey circle in Fig. 18a). In contrast, a relatively low HNO_3 uptake is noted when STS (liquid-NAT mixture) preceded the ice formation which is marked with the green circle (red circle) in Fig. 18(a). In the case of H_2O uptake, a good correlation is found between MLS ΔH_2O and CLaMS ΔH_2O, with a correlation coefficient (R) of 0.76 and a coefficient of determination (R^2) of 0.5776 (Fig. 18b).

4.5.10 Relative percentage contribution of ice formation pathways

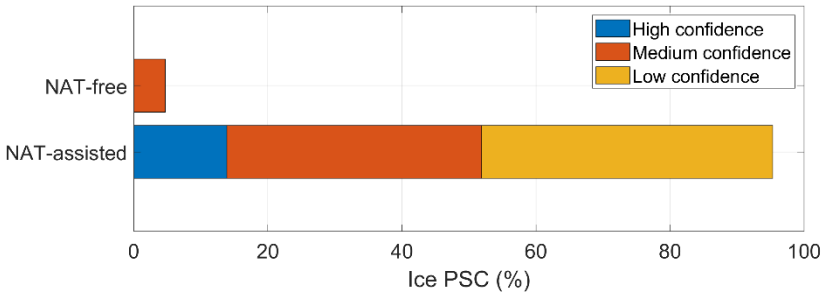

Figure 19. The percentage of ice PSCs formed via NAT-assisted and NAT-free nucleation processes, categorized by confidence levels based on backward trajectory observations and MLS HNO_3 availability. The bars represent

high, medium, and low confidence cases for each process, with confidence levels determined by the presence of NAT and gas-phase HNO_3 concentrations along the trajectories.

Based on the Lagrangian backward trajectory analysis and availability of gas-phase HNO_3 as observed through MLS, we estimated the relative percentage contributions of NAT-assisted and NAT-free ice formation processes, with the color-coded bars indicating different confidence levels based on observational evidence and shown in Fig 19. High confidence (blue) in NAT-assisted formation indicates that direct CALIPSO observational evidence of liquid-NAT mixture was found along the backward trajectory of the ice PSC. This provides strong evidence that the ice formed through NAT-assisted nucleation. Ice PSCs which formed via the NAT-assisted nucleation process are classified with medium confidence (orange) when there is no direct observation of NAT, but significant availability of gas-phase MLS HNO_3 >3 ppb during the observation of NC/STS along the backward trajectory. In this case, even without the detection of NAT, the availability of HNO_3 strongly suggests that NAT could have formed, justifying a medium confidence classification for NAT-assisted nucleation. Low confidence (yellow) in NAT-assisted formation corresponds to cases where the MLS HNO_3 mixing ratio during NC/STS observations was between 0.5 and 3 ppb. While NAT formation cannot be ruled out, the lower HNO_3 mixing ratio suggests only a low likelihood of NAT's involvement. Hence classifying these types of cases to NAT-assisted nucleation with low confidence. These results on ice formation pathways are result of analysis carried using total of 5049 backward trajectories of ice PSC. Out of which, 4796 backward trajectories correspond to the ice formed through the NAT-assisted formation pathway and only 253 trajectories to the NAT-free formation pathway.

Ice PSCs which formed during extreme denitrified conditions are classified as NAT-free ice formation with medium confidence. Here, the backward trajectories reveal very low MLS HNO_3 (<0.5 ppb), creating conditions where NAT formation is unlikely, and ice must have nucleated without the presence of NAT. In this scenario, ice PSCs are likely formed on STS particles with foreign nuclei inclusion. This breakdown helps to clarify the processes of ice formation under varying atmospheric conditions and enhances our understanding of the role NAT plays in polar stratospheric cloud nucleation. The clear separation into different confidence levels also emphasizes the influence of gas-phase HNO_3 availability on determining the nucleation pathway.

In summary, we report the strong enhancement in aerosol loading in the lower stratosphere caused by the black summer event during early 2020. In addition, we observed increased gas-phase MLS HNO_3 and H_2O mixing ratio at an altitude of ~25 km and ~17 km respectively. The increased HNO_3 is due to enhanced heterogeneous reaction known as N_2O_5 hydrolysis while increased H_2O is directly injected by smoke plumes from the bushfire. Subsequently, during Austral Winter 2020, anomalously high PSC areal coverage was observed, suggesting that the modified stratospheric composition of trace gases strongly influenced the PSC formation. Despite of relatively high availability of gas–phase HNO_3 during this period compared to previous normal years, the liquid–NAT mixture PSC remained within one standard deviation with respect to the background mean (2009─2019) while the ice PSC areal coverage exceeded three standard deviations. To explain this behavior, we calculated the 48 h backward trajectories of ice and liquid-NAT mixture PSCs using the CLaMS trajectory module with hourly ERA5 operational analysis meteorological data. The temperature history, uptakes of MLS HNO_3, H_2O mixing ratio during the formation of these ice/liquid–NAT mixture PSCs, and types of PSC observed before the observation of these PSCs along the trajectories are studied to understand their formation pathways. Through this analysis, we

report that 79 % of the liquid-NAT mixture formed via ice-free nucleation pathway accounts with high confidence, as ice PSC has not observed along the trajectory as well as the temperature of the air parcel never decreased 1.5 K below T_{ice} (i.e., the minimum temperature required for ice formation) from the time of observation of 'No Cloud (NC)'/STS till liquid-NAT mixture observation along the backward trajectory. This confirms no formation of ice before the observation of the liquid-NAT mixture. Whereas we report 12 % of the liquid-NAT mixture formed via ice-assisted nucleation pathway with high confidence as ice PSC is observed through CALIPSO before the formation of liquid-NAT mixture along the trajectory and 9 % with low confidence as there is no direct CALIPSO observation of ice PSC before the liquid-NAT mixture but the corresponding temperature decreased 1.5 K below T_{ice}, indicating a possible involvement of ice during this liquid-NAT mixture formation. The inability of the ERA5 operational analysis to capture the small-scale temperature fluctuations caused by the gravity wave and possible bias in ERA5 temperature may contribute uncertainty to these percentage contributions of formation pathways.

In the case of ice formation, we observed that the depolarization ratio at 532 nm of ice PSCs preceded by STS along the trajectories exhibited bimodal distribution. The low depolarization ratio mode peaked at 0.07, and the high depolarization ratio mode peaked at 0.26. In contrast, the ice PSC preceded by liquid-NAT mixture along the trajectory exhibited a single mode of depolarization ratio with a peak occurring at 0.35 which is closer to the high depolarization ratio mode of ice PSC preceded by STS. This hints that ice with a high depolarization ratio could be a result of the nucleation of ice on NAT particles and low depolarization ratio to nucleation of ice on STS which is supported by a previous study from Voigt et al., (2018). To check this, we analyzed the availability of gas-phase HNO_3 at the time of observation of STS, which was observed before ice formation along the backward trajectories, as HNO_3 availability is crucial for NAT formation. The results indicate that ice PSCs with low depolarization ratios formed under denitrified conditions, where the MLS HNO_3 mixing ratio was below 0.5 ppb during the STS observation along the backward trajectories. In these conditions, NAT particles could not form due to low HNO_3 availability which is also confirmed by the CLaMS box model run and resulted in ice nucleating directly on STS. In contrast, ice PSCs with high depolarization ratios formed under normal conditions, where the MLS HNO_3 mixing ratio exceeded 3 ppb during the STS observation. This enough availability of gas-phase HNO_3 led to the formation of NAT particles (again, this is also confirmed by the CLaMS box model run) and led to ice nucleating on NAT. Hence, based on the availability of gas-phase MLS HNO_3 and temperature history, we conclude the ice formation pathways and relative percentage contribution of formation pathways and degree of confidence.

Hence, we report that 14 % of the ice is formed through NAT-assisted ice formation with high confidence as direct CALIPSO observations of liquid-NAT mixtures are present along the trajectory. And 38 % with medium confidence, as there is significant gas-phase MLS HNO_3 (>3 ppb) suggesting possible NAT formation before the ice formation. And 43 % with low confidence when HNO_3 levels are between 0.5 and 3 ppb, indicating a lower likelihood of NAT formation. Furthermore, we report that only 5 % of ice formed through NAT-free ice formation with medium confidence, as they are formed under extremely denitrified conditions (HNO_3 < 0.5 ppb), suggesting less likelihood of NAT formation and thus ice formed through nucleating on STS. This suggests the availability of the gas-phase HNO_3 is a crucial factor in deciding whether ice forms through a NAT-assisted or NAT-free nucleation process. To the best of our knowledge, this is the first study which provides relative contributions of various liquid-NAT mixtures and ice formation pathways. These results provide deeper insights into the

microphysical processes through which the aerosols from extreme bushfire events (like black summer) can influence stratospheric chemistry and PSC formation.

5 Conclusions

Australia's extreme bushfire event of 2019/20, also referred to as black summer, injected 0.4 to 2 Tg of aerosols into the stratosphere, initiating a series of events. We carried out an extensive investigation on the impacts of bushfire emissions on the Polar Stratospheric Clouds (PSCs), using multi-satellite and reanalyses data. In addition, to explain the anomaly observed in ice and liquid-NAT mixture PSC areal coverage, we studied the formation pathways of these PSCs by analyzing temperature history, availability of gas-phase HNO_3, along with CLaMS microphysical box model simulation and retrieved the relative percentage contribution of formation pathways of ice and liquid-NAT mixture PSCs. The key findings from this study are:

1. During the austral autumn of 2020, we found a significant increase in gas phase nitric acid (HNO_3) and water vapor (H_2O) (principal constituents of PSCs) from MLS measurement in high latitude region of the southern hemisphere at the altitudes of ~25 and ~17 km respectively. The former is due to the enhanced dinitrogen pentoxide hydrolysis process, caused by the increased bushfire aerosols. The latter is attributed to the direct injection of water vapor by the black summer event.

2. The increase in HNO_3 was expected to enhance HNO_3-containing PSCs like STS and NAT. While the areal coverage of STS peaked significantly, no notable enhancement in liquid-NAT mixtures was observed. However, there was an anomalous increase in the areal coverage of ice PSC.

3. We report 79 % of liquid-NAT mixtures formed through ice-free nucleation with high confidence, as no ice PSCs were observed along the backward trajectories and temperature remained above the ice formation threshold (T_{ice}-1.5K). Whereas 12 % of liquid-NAT mixtures formed via ice-assisted nucleation with high confidence, as CALIPSO observations of ice PSCs before liquid-NAT formation, and 9 % with low confidence, as the temperature dropped below the ice formation threshold but no direct ice PSC observation.

4. We observed the bimodal distribution of depolarization ratio at 532 nm of ice PSCs which are preceded by STS along the backward trajectories. Further analysis of this revealed that the low depolarization ratio mode (peaked at ~0.07) corresponds to ice nucleation on STS under denitrified conditions (HNO_3 < 0.5 ppb). A high depolarization ratio (peaked ~0.26) corresponds to ice nucleation on NAT under normal conditions (HNO_3 > 3 ppb).

5. We report 14 % of ice PSCs formed via NAT-assisted nucleation with high confidence, as the presence of liquid-NAT mixtures is observed through CALIPSO along the backward trajectory of these ice PSCs and 38 % with medium confidence, as there is no direct CALIPSO observation of present of liquid-NAT mixture but significant HNO_3 availability > 3 ppb, hence high likelihood of NAT formation, and 43 % with low confidence, HNO_3 levels between 0.5 and 3 ppb, relatively low likelihood of the NAT. Thus, NAT-assisted ice formation pathway accounts for ~95 % of ice PSC. And just 5 % of ice PSCs formed via NAT-free nucleation under extremely denitrified conditions (HNO_3 < 0.5 ppb), as not enough HNO_3 availability for NAT formation, and thus these ice PSCs should have nucleated on STS with the possible inclusion of foreign nuclei. These results suggest the ice formation pathway is also decided by the gas-phase HNO_3 availability.

In the context of climate change scenarios, a warming troposphere and cooling stratosphere are expected. The former is expected to increase the frequency of extreme wildfire events, and the latter is projected to enhance the PSC areal coverage, together possibly delaying the ozone recovery process. The findings from this study will contribute to a deeper understanding of the influence of extreme wildfire events on PSC dynamics.

Data availability

Processed data are available upon request.

Author contribution

SP conceived the work and carried out the scientific data analysis. SP, NSA, KS, KKM, and SKS were involved in the scientific interpretation of the results, leading to the formulation of the manuscript. SP prepared the initial draft with input from NSA. All authors reviewed the manuscript.

Competing interests

The authors declare that they have no conflict of interest.

Acknowledgements.

We acknowledge the mission scientists of OMPS (for aerosol extinction coefficient, and temperature), MLS (for HNO_3, and H_2O mixing ratio), ACE-FTS (for HNO_3, H_2O, HF, and N_2O_5 mixing ratio), ERA5 (for meteorological data), CALIPSO (for PSCs) and the associated personnel for the data used in this work. In addition, we acknowledge the CLaMS team for the model used in this work.

Financial support

One of the authors (SP) would like to thank the Centre for Research, Christ University for their support during this work. One of the authors (SKS) would like to thank SERB-DST for the J. C. Bose Fellowship. One of the authors (NSA) is supported by the DST in the form of an INSPIRE Faculty Fellowship (faculty registration number: IFA20-EAS-83). We thank the Divecha Centre for Climate Change for supporting this work.

Review statement

We thank the five anonymous reviewers and Dr. Farahnaz Khosrawi for helping to improve the paper.

References

Allen, D. R., Fromm, M. D., Kablick III, G. P., and Nedoluha, G. E.: Smoke with induced rotation and lofting (SWIRL) in the stratosphere, J. Atmos. Sci., 77, 4297–4316, 2020.

Ansmann, A., Ohneiser, K., Chudnovsky, A., Knopf, D. A., Eloranta, E. W., Villanueva, D., Seifert, P., Radenz, M., Barja, B., Zamorano, F., Jimenez, C., Engelmann, R., Baars, H., Griesche, H., Hofer, J., Althausen, D., and Wandinger, U.: Ozone depletion in the Arctic and Antarctic stratosphere induced by wildfire smoke, Atmos. Chem. Phys., 22, 11701–11726, https://doi.org/10.5194/ACP-22-11701-2022, 2022.

Bernath, P. F., Steffen, J., Crouse, J., and Boone, C. D.: Atmospheric Chemistry Experiment SciSat Level 2 Processed Data, v4.0, 2020.

Bogdan, A. and Kulmala, M.: Aerosol silica as a possible candidate for the heterogeneous formation of nitric acid hydrates in the stratosphere, Geophys. Res. Lett., 26, 1433–1436, 1999.

Bogdan, A., Molina, M. J., Kulmala, M., MacKenzie, A. R., and Laaksonen, A.: Study of finely divided aqueous systems as an aid to understanding the formation mechanism of polar stratospheric clouds: Case of HNO3/H2O and H2SO4/H2O systems, J. Geophys. Res.-Atmos., 108, 2003.

Brewer, A. W.: Evidence for a world circulation provided by the measurements of helium and water vapour distribution in the stratosphere, Q. J. R. Meteorol. Soc., 75, 351–363, https://doi.org/10.1002/QJ.49707532603, 1949.

Butchart, N.: The Brewer-Dobson circulation, Rev. Geophys., 52, 157–184, https://doi.org/10.1002/2013RG000448, 2014.

Carslaw, K. S., Luo, B. P., Clegg, S. L., Peter, T., Brimblecombe, P., and Crutzen, P. J.: Stratospheric aerosol growth and HNO3 gas phase depletion from coupled HNO3 and water uptake by liquid particles, Geophys. Res. Lett., 21, 2479–2482, https://doi.org/10.1029/94GL02799, 1994.

Carslaw, K. S., Wirth, M., Tsias, A., Luo, B. P., Dörnbrack, A., Leutbecher, M., Volkert, H., Renger, W., Bacmeister, J. T., and Peter, T.: Particle microphysics and chemistry in remotely observed mountain polar stratospheric clouds, J. Geophys. Res.-Atmos., 103, 5785–5796, 1998.

Carslaw, K. S., Peter, T., Bacmeister, J. T., and Eckermann, S. D.: Widespread solid particle formation by mountain waves in the Arctic stratosphere, J. Geophys. Res.-Atmos., 104, 1827–1836, https://doi.org/10.1029/1998JD100033, 1999.

Chang, D. Y., Yoon, J., Lelieveld, J., Park, S. K., Yum, S. S., Kim, J., and Jeong, S.: Direct radiative forcing of biomass burning aerosols from the extensive Australian wildfires in 2019–2020, Environ. Res. Lett., 16, 044041, https://doi.org/10.1088/1748-9326/ABECFE, 2021.

Curtius, J., Weigel, R., Vössing, H.-J., Wernli, H., Werner, A., Volk, C.-M., Konopka, P., Krebsbach, M., Schiller, C., and Roiger, A.: Observations of meteoric material and implications for aerosol nucleation in the winter Arctic lower stratosphere derived from in situ particle measurements, Atmos. Chem. Phys., 5, 3053–3069, 2005.

Cziczo, D. J., Thomson, D. S., and Murphy, D. M.: Ablation, Flux, and Atmospheric Implications of Meteors Inferred from Stratospheric Aerosol, Science (1979), 291, 1772–1775, https://doi.org/10.1126/SCIENCE.1057737, 2001.

Deb, P., Moradkhani, H., Abbaszadeh, P., Kiem, A. S., Engström, J., Keellings, D., and Sharma, A.: Causes of the Widespread 2019–2020 Australian Bushfire Season, Earths Future, 8, e2020EF001671, https://doi.org/https://doi.org/10.1029/2020EF001671, 2020.

Engel, I., Luo, B. P., Pitts, M. C., Poole, L. R., Hoyle, C. R., Grooß, J. U., Dörnbrack, A., and Peter, T.: Heterogeneous formation of polar stratospheric clouds-Part 2: Nucleation of ice on synoptic scales, Atmos. Chem. Phys., 13, 10769–10785, https://doi.org/10.5194/ACP-13-10769-2013, 2013.

Fortin, T. J., Drdla, K., Iraci, L. T., and Tolbert, M. A.: Ice condensation on sulfuric acid tetrahydrate: Implications for polar stratospheric ice clouds, Atmos. Chem. Phys., 3, 987–997, 2003.

Fueglistaler, S., Dessler, A. E., Dunkerton, T. J., Folkins, I., Fu, Q., and Mote, P. W.: Tropical tropopause layer, Rev. Geophys., 47, https://doi.org/10.1029/2008RG000267, 2009.

Gao, R. S., Gierczak, T., Thornberry, T. D., Rollins, A. W., Burkholder, J. B., Telg, H., Voigt, C., Peter, T., and Fahey, D. W.: Persistent Water-Nitric Acid Condensate with Saturation Water Vapor Pressure Greater than That of Hexagonal Ice, J. Phys. Chem. A, 120, 1431–1440, https://doi.org/10.1021/ACS.JPCA.5B06357/ASSET/IMAGES/MEDIUM/JP-2015-063578_0010.GIF, 2016.

Grooß, J. U., Konopka, P., and Müller, R.: Ozone Chemistry during the 2002 Antarctic Vortex Split, J Atmos Sci, 62, 860–870, https://doi.org/10.1175/JAS-3330.1, 2005.

Grooß, J. U., Engel, I., Borrmann, S., Frey, W., Günther, G., Hoyle, C. R., Kivi, R., Luo, B. P., Molleker, S., Peter, T., Pitts, M. C., Schlager, H., Stiller, G., Vömel, H., Walker, K. A., and Müller, R.: Nitric acid trihydrate nucleation and denitrification in the Arctic stratosphere, Atmos. Chem. Phys., 14, 1055–1073, https://doi.org/10.5194/ACP-14-1055-2014, 2014.

Hanson, D. and Mauersberger, K.: Laboratory studies of the nitric acid trihydrate: Implications for the south polar stratosphere, Geophys. Res. Lett., 15, 855–858, https://doi.org/10.1029/GL015I008P00855, 1988.

Hanson, D. R. and Ravishankara, A. R.: The reaction probabilities of ClONO2 and N2O5 on 40 to 75% sulfuric acid solutions, J. Geophys. Res.-Atmos., 96, 17307–17314, https://doi.org/10.1029/91JD01750, 1991.

Hanson, D. R. and Ravishankara, A. R.: Investigation of the reactive and nonreactive processes involving nitryl hypochlorite and hydrogen chloride on water and nitric acid doped ice, J. Phys. Chem., 96, 2682–2691, 1992.

Heinold, B., Baars, H., Barja, B., Christensen, M., Kubin, A., Ohneiser, K., Schepanski, K., Schutgens, N., Senf, F., and Schrödner, R.: Important role of stratospheric injection height for the distribution and radiative forcing of smoke aerosol from the 2019/2020 Australian wildfires, Atmos. Chem. Phys., 1–20, 2022.

Hersbach, H., Bell, B., Berrisford, P., Hirahara, S., Horányi, A., Muñoz-Sabater, J., Nicolas, J., Peubey, C., Radu, R., Schepers, D., Simmons, A., Soci, C., Abdalla, S., Abellan, X., Balsamo, G., Bechtold, P., Biavati, G., Bidlot, J., Bonavita, M., De Chiara, G., Dahlgren, P., Dee, D., Diamantakis, M., Dragani, R., Flemming, J., Forbes, R., Fuentes, M., Geer, A., Haimberger, L., Healy, S., Hogan, R. J., Hólm, E., Janisková, M., Keeley, S., Laloyaux, P., Lopez, P., Lupu, C., Radnoti, G., de Rosnay, P., Rozum, I., Vamborg, F., Villaume, S., and Thépaut, J. N.: The ERA5 global reanalysis, Q. J. R. Meteorol. Soc., 146, 1999–2049, https://doi.org/10.1002/QJ.3803, 2020.

Hirsch, E. and Koren, I.: Record-breaking aerosol levels explained by smoke injection into the stratosphere, Science (1979), 371, 1269–1274, 2021.

Höpfner, M., Luo, B. P., Massoli, P., Cairo, F., Spang, R., Snels, M., Di Donfrancesco, G., Stiller, G., Von Clarmann, T., and Fischer, H.: Spectroscopic evidence for NAT, STS, and ice in MIPAS infrared limb emission measurements of polar stratospheric clouds, Atmos. Chem. Phys., 6, 1201–1219, 2006.

Hoyle, C. R., Engel, I., Luo, B. P., Pitts, M. C., Poole, L. R., Grooß, J. U., and Peter, T.: Heterogeneous formation of polar stratospheric clouds-Part 1: Nucleation of nitric acid trihydrate (NAT), Atmos. Chem. Phys., 13, 9577–9595, https://doi.org/10.5194/ACP-13-9577-2013, 2013.

Iannarelli, R. and Rossi, M. J.: The mid-IR Absorption Cross Sections of α- and β-NAT (HNO3 · 3H2O) in the range 170 to 185 K and of metastable NAD (HNO3 · 2H2O) in the range 172 to 182 K, J. Geophys. Res.-Atmos., 120, 11,707-11,727, https://doi.org/10.1002/2015JD023903, 2015.

Iraci, L. T., Middlebrook, A. M., and Tolbert, M. A.: Laboratory studies of the formation of polar stratospheric clouds: Nitric acid condensation on thin sulfuric acid films, J. Geophys. Res.-Atmos., 100, 20969–20977, https://doi.org/10.1029/95JD02267, 1995.

Junge, C. E., Chagnon, C. W., and Manson, J. E.: STRATOSPHERIC AEROSOLS, Journal of Atmospheric Sciences, 18, 81–108, https://doi.org/https://doi.org/10.1175/1520-0469(1961)018<0081:SA>2.0.CO;2, 1961.

Kessenich, H. E., Seppälä, A., and Rodger, C. J.: Potential drivers of the recent large Antarctic ozone holes, Nat. Commun., 2023 14:1, 14, 1–9, https://doi.org/10.1038/s41467-023-42637-0, 2023.

Khaykin, S., Legras, B., Bucci, S., Sellitto, P., Isaksen, L., Tence, F., Bekki, S., Bourassa, A., Rieger, L., and Zawada, D.: The 2019/20 Australian wildfires generated a persistent smoke-charged vortex rising up to 35 km altitude, Commun. Earth. Environ., 1, 1–12, 2020.

Khosrawi, F., Urban, J., Pitts, M. C., Voelger, P., Achtert, P., Kaphlanov, M., Santee, M. L., Manney, G. L., Murtagh, D., and Fricke, K. H.: Denitrification and polar stratospheric cloud formation during the Arctic winter 2009/2010, Atmos. Chem. Phys., 11, 8471–8487, https://doi.org/10.5194/ACP-11-8471-2011, 2011.

Khosrawi, F., Urban, J., Lossow, S., Stiller, G., Weigel, K., Braesicke, P., Pitts, M. C., Rozanov, A., Burrows, J. P., and Murtagh, D.: Sensitivity of polar stratospheric cloud formation to changes in water vapour and temperature, Atmos. Chem. Phys., 16, 101–121, https://doi.org/10.5194/ACP-16-101-2016, 2016.

Klekociuk, A. R., Tully, M. B., Krummel, P. B., Henderson, S. I., Smale, D., Querel, R., Nichol, S., Alexander, S. P., Fraser, P. J., and Nedoluha, G.: The Antarctic ozone hole during 2020, J. South. Hemisph. Earth Syst. Sci., 72, 19–37, https://doi.org/10.1071/ES21015, 2022.

Kondragunta, S., Flynn, L. E., Neuendorffer, A., Miller, A. J., Long, C., Nagatani, R., Zhou, S., Beck, T., Beach, E., and McPeters, R.: Vertical structure of the anomalous 2002 Antarctic ozone hole, J. Atmos. Sci., 62, 801–811, 2005.

Konopka, P., Steinhorst, H. M., Grooß, J. U., Günther, G., Müller, R., Elkins, J. W., Jost, H. J., Richard, E., Schmidt, U., Toon, G., and McKenna, D. S.: Mixing and ozone loss in the 1999–2000 Arctic vortex: Simulations with the three-dimensional Chemical Lagrangian Model of the Stratosphere (CLaMS), J. Geophys. Res.-Atmos., 109, 2315, https://doi.org/10.1029/2003JD003792, 2004.

Koop, T., Biermann, U. M., Raber, W., Luo, B. P., Crutzen, P. J., and Peter, T.: Do stratospheric aerosol droplets freeze above the ice frost point?, Geophys. Res. Lett., 22, 917–920, https://doi.org/10.1029/95GL00814, 1995.

Koop, T., Luo, B., Biermann, U. M., Crutzen, P. J., and Peter, T.: Freezing of HNO3/H2SO4/H2O Solutions at Stratospheric Temperatures: Nucleation Statistics and Experiments, J. Phys. Chem. A, 101, 1117–1133, https://doi.org/10.1021/jp9626531, 1997.

Koop, T., Ng, H. P., Molina, L. T., and Molina, M. J.: A New Optical Technique to Study Aerosol Phase Transitions: The Nucleation of Ice from H2SO4 Aerosols, J. Phys. Chem. A, 102, 8924–8931, https://doi.org/10.1021/jp9828078, 1998.

Koop, T., Luo, B., Tsias, A., and Peter, T.: Water activity as the determinant for homogeneous ice nucleation in aqueous solutions, Nature 2000 406:6796, 406, 611–614, https://doi.org/10.1038/35020537, 2000.

Lambert, A., Santee, M. L., Wu, D. L., and Chae, J. H.: A-train CALIOP and MLS observations of early winter Antarctic polar stratospheric clouds and nitric acid in 2008, Atmos. Chem. Phys., 12, 2899–2931, https://doi.org/10.5194/ACP-12-2899-2012, 2012.

Lambert, A., Santee, M. L., and Livesey, N. J.: Interannual variations of early winter Antarctic polar stratospheric cloud formation and nitric acid observed by CALIOP and MLS, Atmos. Chem. Phys., 16, 15219–15246, https://doi.org/10.5194/ACP-16-15219-2016, 2016.

Larsen, N., Knudsen, B. M., Rosen, J. M., Kjome, N. T., Neuber, R., and Kyrö, E.: Temperature histories in liquid and solid polar stratospheric cloud formation, J. Geophys. Res.-Atmos., 102, 23505–23517, https://doi.org/10.1029/97JD01666, 1997.

Li, D., Wang, Z., Li, S., Zhang, J., and Feng, W.: Climatology of Polar Stratospheric Clouds Derived from CALIPSO and SLIMCAT, Remote. Sens. (Basel), 16, 3285, https://doi.org/10.3390/RS16173285/S1, 2024.

Li, M., Shen, F., and Sun, X.: 2019–2020 Australian bushfire air particulate pollution and impact on the South Pacific Ocean, Sci. Rep. 2021 11:1, 11, 1–13, https://doi.org/10.1038/s41598-021-91547-y, 2021.

Liu, G., Hirooka, T., Eguchi, N., and Krüger, K.: Dynamical evolution of a minor sudden stratospheric warming in the Southern Hemisphere in 2019, Atmos. Chem. Phys., 22, 3493–3505, https://doi.org/10.5194/ACP-22-3493-2022, 2022.

Lowe, D. and MacKenzie, A. R.: Polar stratospheric cloud microphysics and chemistry, J. Atmos. Sol. Terr. Phys., 70, 13–40, https://doi.org/10.1016/J.JASTP.2007.09.011, 2008.

Luo, B. P., Voigt, C., Fueglistaler, S., and Peter, T.: Extreme NAT supersaturations in mountain wave ice PSCs: A clue to NAT formation, J. Geophys. Res.-Atmos., 108, 4441, https://doi.org/10.1029/2002JD003104, 2003.

Mansoor, S., Farooq, I., Kachroo, M. M., Mahmoud, A. E. D., Fawzy, M., Popescu, S. M., Alyemeni, M. N., Sonne, C., Rinklebe, J., and Ahmad, P.: Elevation in wildfire frequencies with respect to the climate change, J. Environ. Manage., 301, 113769, Https://doi.org/10.1016/J.JENVMAN.2021.113769, 2022.

Marti, J. and Mauersberger, K.: A survey and new measurements of ice vapor pressure at temperatures between 170 and 250K, Geophys. Res. Lett., 20, 363–366, https://doi.org/10.1029/93GL00105, 1993.

McKenna, D. S., Konopka, P., Grooß, J.-U., Günther, G., Müller, R., Spang, R., Offermann, D., and Orsolini, Y.: A new Chemical Lagrangian Model of the Stratosphere (CLaMS) 1. Formulation of advection and mixing, J. Geophys. Res.-Atmos., 107, ACH 15-1, https://doi.org/10.1029/2000JD000114, 2002a.

McKenna, D. S., Grooß, J. U., Günther, G., Konopka, P., Müller, R., Carver, G., and Sasano, Y.: A new Chemical Lagrangian Model of the Stratosphere (CLaMS) 2. Formulation of chemistry scheme and initialization, J. Geophys. Res.-Atmos., 107, ACH 4-1, https://doi.org/10.1029/2000JD000113, 2002b.

Molina, M. J. and Rowland, F. S.: Stratospheric sink for chlorofluoromethanes: chlorine atom-catalysed destruction of ozone, Nature, 249, 810–812, 1974.

Molina, M. J., Zhang, R., Wooldridge, P. J., McMahon, J. R., Kim, J. E., Chang, H. Y., and Beyer, K. D.: Physical chemistry of the H2SO4/HNO 3/H2O system: Implications for polar stratospheric clouds, Science (1979), 261, 1418–1423, https://doi.org/10.1126/SCIENCE.261.5127.1418, 1993a.

Molina, M. J., Zhang, R., Wooldridge, P. J., McMahon, J. R., Kim, J. E., Chang, H. Y., and Beyer, K. D.: Physical chemistry of the H2SO4/HNO3/H2O system: Implications for polar stratospheric clouds, Science (1979), 261, 1418–1423, 1993b.

Müller, R., Crutzen, P. J., Grooß, J.-U., Brühl, C., Russell III, J. M., and Tuck, A. F.: Chlorine activation and ozone depletion in the Arctic vortex: Observations by the Halogen Occultation Experiment on the Upper Atmosphere Research Satellite, J. Geophys. Res.-Atmos., 101, 12531–12554, https://doi.org/https://doi.org/10.1029/95JD00220, 1996.

Müller, R., Crutzen, P. J., Grooβ, J.-U., Bürhl, C., Russell, J. M., Gernandt, H., McKenna, D. S., and Tuck, A. F.: Severe chemical ozone loss in the Arctic during the winter of 1995–96, Nature, 389, 709–712, https://doi.org/10.1038/39564, 1997.

Murphy, D. M., Froyd, K. D., Schwarz, J. P., and Wilson, J. C.: Observations of the chemical composition of stratospheric aerosol particles, Q. J. R. Meteorol. Soc., 140, 1269–1278, 2014.

Nakajima, H., Wohltmann, I., Wegner, T., Takeda, M., Pitts, M. C., Poole, L. R., Lehmann, R., Santee, M. L., and Rex, M.: Polar stratospheric cloud evolution and chlorine activation measured by CALIPSO and MLS, and modeled by ATLAS, Atmos. Chem. Phys., 16, 3311–3325, https://doi.org/10.5194/ACP-16-3311-2016, 2016.

Ohneiser, K., Ansmann, A., Kaifler, B., Chudnovsky, A., Barja, B., Knopf, D. A., Kaifler, N., Baars, H., Seifert, P., Villanueva, D., Jimenez, C., Radenz, M., Engelmann, R., Veselovskii, I., and Zamorano, F.: Australian wildfire smoke in the stratosphere: the decay phase in 2020/2021 and impact on ozone depletion, Atmos. Chem. Phys., 22, 7417–7442, https://doi.org/10.5194/acp-22-7417-2022, 2022.

Peter, T.: Microphysics and heterogeneous chemistry of polar stratospheric clouds, 48, 785–822, https://doi.org/10.1146/annurev.physchem.48.1.785, 1997.

Peter, T. and Grooß, J.-U.: Stratospheric ozone depletion and climate change, R. Soc. Chem., 108–144 pp., 2012.

Pitts, M. C., Thomason, L. W., Poole, L. R., and Winker, D. M.: Characterization of polar stratospheric clouds with spaceborne lidar: CALIPSO and the 2006 antarctic season, Atmos. Chem. Phys., 7, 5207–5228, https://doi.org/10.5194/ACP-7-5207-2007, 2007.

Pitts, M. C., Poole, L. R., and Thomason, L. W.: CALIPSO polar stratospheric cloud observations: Second-generation detection algorithm and composition discrimination, Atmos. Chem. Phys., 9, 7577–7589, https://doi.org/10.5194/ACP-9-7577-2009, 2009.

Pitts, M. C., Poole, L. R., Lambert, A., and Thomason, L. W.: An assessment of CALIOP polar stratospheric cloud composition classification, Atmos. Chem. Phys., 13, 2975–2988, https://doi.org/10.5194/ACP-13-2975-2013, 2013.

Pitts, M. C., Poole, L. R., and Gonzalez, R.: Polar stratospheric cloud climatology based on CALIPSO spaceborne lidar measurements from 2006 to 2017, Atmos. Chem. Phys., 18, 10881–10913, https://doi.org/10.5194/ACP-18-10881-2018, 2018.

Ploeger, F., Diallo, M., Charlesworth, E., Konopka, P., Legras, B., Laube, J. C., Grooß, J.-U., Günther, G., Engel, A., and Riese, M.: The stratospheric Brewer–Dobson circulation inferred from age of air in the ERA5 reanalysis, Atmos. Chem. Phys., 21, 8393–8412, 2021.

Ravishankara, A. R. and Hanson, D. R.: Differences in the reactivity of type I polar stratospheric clouds depending on their phase, J. Geophys. Res.-Atmos., 101, 3885–3890, https://doi.org/10.1029/95JD03009, 1996a.

Ravishankara, A. R. and Hanson, D. R.: Differences in the reactivity of type I polar stratospheric clouds depending on their phase, J. Geophys. Res.-Atmos., 101, 3885–3890, 1996b.

Rex, M., Salawitch, R. J., von der Gathen, P., Harris, N. R. P., Chipperfield, M. P., and Naujokat, B.: Arctic ozone loss and climate change, Geophys. Res. Lett., 31, 2004.

Rieger, L. A., Randel, W. J., Bourassa, A. E., and Solomon, S.: Stratospheric temperature and ozone anomalies associated with the 2020 Australian New Year Fires, Geophys. Res. Lett., 48, e2021GL095898, 2021.

Robrecht, S., Vogel, B., Grooß, J. U., Rosenlof, K., Thornberry, T., Rollins, A., Krämer, M., Christensen, L., and Müller, R.: Mechanism of ozone loss under enhanced water vapour conditions in the mid-latitude lower stratosphere in summer, Atmos. Chem. Phys., 19, 5805–5833, https://doi.org/10.5194/ACP-19-5805-2019, 2019.

Santee, M. L., Lambert, A., Manney, G. L., Livesey, N. J., Froidevaux, L., Neu, J. L., Schwartz, M. J., Millán, L. F., Werner, F., Read, W. G., Park, M., Fuller, R. A., and Ward, B. M.: Prolonged and Pervasive Perturbations in the Composition of the Southern Hemisphere Midlatitude Lower Stratosphere From the Australian New Year's Fires, Geophys. Res. Lett., 49, e2021GL096270, https://doi.org/10.1029/2021GL096270, 2022a.

Santee, M. L., Lambert, A., Manney, G. L., Livesey, N. J., Froidevaux, L., Neu, J. L., Schwartz, M. J., Millán, L. F., Werner, F., Read, W. G., Park, M., Fuller, R. A., and Ward, B. M.: Prolonged and Pervasive Perturbations in the Composition of the Southern Hemisphere Midlatitude Lower Stratosphere From the Australian New Year's Fires, Geophys. Res. Lett., 49, e2021GL096270, https://doi.org/https://doi.org/10.1029/2021GL096270, 2022b.

Schneider, J., Weigel, R., Klimach, T., Dragoneas, A., Appel, O., Hünig, A., Molleker, S., Köllner, F., Clemen, H.-C., and Eppers, O.: Aircraft-based observation of meteoric material in lower-stratospheric aerosol particles between 15 and 68 N, Atmos. Chem. Phys., 21, 989–1013, 2021.

Schoeberl, M. R., Jensen, E. J., Pfister, L., Ueyama, R., Avery, M., and Dessler, A. E.: Convective Hydration of the Upper Troposphere and Lower Stratosphere, J. Geophys. Res.-Atmos., 123, 4583–4593, https://doi.org/10.1029/2018JD028286, 2018.

Schwartz, M. J., Santee, M. L., Pumphrey, H. C., Manney, G. L., Lambert, A., Livesey, N. J., Millán, L., Neu, J. L., Read, W. G., and Werner, F.: Australian new year's pyrocb impact on stratospheric composition, Geophys. Res. Lett., 47, e2020GL090831, 2020.

Schwarzenböck, A., Mertes, S., Heintzenberg, J., Wobrock, W., and Laj, P.: Impact of the Bergeron–Findeisen process on the release of aerosol particles during the evolution of cloud ice, Atmos Res, 58, 295–313, https://doi.org/https://doi.org/10.1016/S0169-8095(01)00096-5, 2001.

Sellitto, P., Belhadji, R., Kloss, C., and Legras, B.: Radiative impacts of the Australian bushfires 2019–2020–Part 1: Large-scale radiative forcing, Atmos. Chem. Phys., 1–20, 2022.

Solomon, S., Dube, K., Stone, K., Yu, P., Kinnison, D., Toon, O. B., Strahan, S. E., Rosenlof, K. H., Portmann, R., Davis, S., Randel, W., Bernath, P., Boone, C., Bardeen, C. G., Bourassa, A., Zawada, D., and Degenstein, D.: On the stratospheric chemistry of midlatitude wildfire smoke, Proc. Natl. Acad. Sci. U S A, 119, e2117325119, https://doi.org/10.1073/PNAS.2117325119/SUPPL_FILE/PNAS.2117325119.SAPP.PDF, 2022.

Stocker, M., Ladstädter, F., and Steiner, A. K.: Observing the climate impact of large wildfires on stratospheric temperature, Sci. Rep., 11, 22994, https://doi.org/10.1038/s41598-021-02335-7, 2021.

Tabazadeh, A., Turco, R. P., Drdla, K., Jacobson, M. Z., and Toon, O. B.: A study of type I polar stratospheric cloud formation, Geophys. Res. Lett., 21, 1619–1622, 1994.

Taha, G., Loughman, R., Zhu, T., Thomason, L., Kar, J., Rieger, L., and Bourassa, A.: OMPS LP Version 2.0 multi-wavelength aerosol extinction coefficient retrieval algorithm, Atmos. Meas. Tech., 14, 1015–1036, https://doi.org/10.5194/AMT-14-1015-2021, 2021.

Tencé, F., Jumelet, J., Sarkissian, A., Bekki, S., and Khaykin, S.: Optical properties of smoke particules from Australian 2019-20 wildfires derived from lidar measurements at the French Antarctic station Dumont d'Urville, in: EGU General Assembly Conference Abstracts, EGU21-12466, 2021.

Tencé, F., Jumelet, J., Bekki, S., Khaykin, S., Sarkissian, A., and Keckhut, P.: Australian Black Summer Smoke Observed by Lidar at the French Antarctic Station Dumont d'Urville, J. Geophys. Res.-Atmos., 127, e2021JD035349, https://doi.org/10.1029/2021JD035349, 2022.

Thölix, L., Backman, L., Kivi, R., and Karpechko, A. Y.: Variability of water vapour in the Arctic stratosphere, Atmos. Chem. Phys., 16, 4307–4321, https://doi.org/10.5194/ACP-16-4307-2016, 2016.

Thomason, L. W. and Peter, T.: Assessment of stratospheric aerosol properties (ASAP), SPARC report, 2006.

Toon, O. B., Turco, R. P., Jordan, J., Goodman, J., and Ferry, G.: Physical processes in polar stratospheric ice clouds, J. Geophys. Res.-Atmos., 94, 11359–11380, 1989.

Tritscher, I., Grooß, J. U., Spang, R., Pitts, M. C., Poole, L. R., Müller, R., and Riese, M.: Lagrangian simulation of ice particles and resulting dehydration in the polar winter stratosphere, Atmos. Chem. Phys., 19, 543, https://doi.org/10.5194/ACP-19-543-2019, 2019.

Tritscher, I., Pitts, M. C., Poole, L. R., Alexander, S. P., Cairo, F., Chipperfield, M. P., Grooß, J. U., Höpfner, M., Lambert, A., Luo, B., Molleker, S., Orr, A., Salawitch, R., Snels, M., Spang, R., Woiwode, W., and Peter, T.: Polar Stratospheric Clouds: Satellite Observations, Processes, and Role in Ozone Depletion, Rev. Geophys., 59, e2020RG000702, https://doi.org/10.1029/2020RG000702, 2021.

Voigt, C., Schreiner, J., Kohlmann, A., Zink, P., Mauersberger, K., Larsen, N., Deshler, T., Kroger, C., Rosen, J., and Adriani, A.: Nitric acid trihydrate (NAT) in polar stratospheric clouds, Science (1979), 290, 1756–1758, 2000.

Voigt, C., Schlager, H., Luo, B. P., Dörnbrack, A., Roiger, A., Stock, P., Curtius, J., Vössing, H., Borrmann, S., and Davies, S.: Nitric acid trihydrate (NAT) formation at low NAT supersaturation in polar stratospheric clouds (PSCs), Atmos. Chem. Phys., 5, 1371–1380, 2005.

Voigt, C., Dörnbrack, A., Wirth, M., Groß, S. M., Pitts, M. C., Poole, L. R., Baumann, R., Ehard, B., Sinnhuber, B. M., Woiwode, W., and Oelhaf, H.: Widespread polar stratospheric ice clouds in the 2015-2016 Arctic winter - Implications for ice nucleation, Atmos. Chem. Phys., 18, 15623–15641, https://doi.org/10.5194/ACP-18-15623-2018, 2018.

Wang, P., Solomon, S., and Stone, K.: Stratospheric chlorine processing after the 2020 Australian wildfires derived from satellite data, Proc. Natl. Acad. Sci. U S A, 120, e2213910120, https://doi.org/10.1073/PNAS.2213910120/SUPPL_FILE/PNAS.2213910120.SAPP.PDF, 2023.

Waters, J. W., Froidevaux, L., Harwood, R. S., Jarnot, R. F., Pickett, H. M., Read, W. G., Siegel, P. H., Cofield, R. E., Filipiak, M. J., Flower, D. A., Holden, J. R., Lau, G. K., Livesey, N. J., Manney, G. L., Pumphrey, H. C., Santee, M. L., Wu, D. L., Cuddy, D. T., Lay, R. R., Loo, M. S., Perun, V. S., Schwartz, M. J., Stek, P. C., Thurstans, R. P., Boyles, M. A., Chandra, K. M., Chavez, M. C., Chen, G. S., Chudasama, B. V., Dodge, R., Fuller, R. A., Girard, M. A., Jiang, J. H., Jiang, Y., Knosp, B. W., Labelle, R. C., Lam, J. C., Lee, K. A., Miller, D., Oswald, J. E., Patel, N. C., Pukala, D. M., Quintero, O., Scaff, D. M., Van Snyder, W., Tope, M. C., Wagner, P. A., and Walch, M. J.: The Earth Observing System Microwave Limb Sounder (EOS MLS) on the aura satellite, IEEE Trans. Geosci. Remote Sens., 44, 1075–1092, https://doi.org/10.1109/TGRS.2006.873771, 2006.

Weiss, F., Kubel, F., Gálvez, Ó., Hoelzel, M., Parker, S. F., Baloh, P., Iannarelli, R., Rossi, M. J., and Grothe, H.: Metastable Nitric Acid Trihydrate in Ice Clouds, Angewandte Chemie International Edition, 55, 3276–3280, https://doi.org/10.1002/ANIE.201510841, 2016.

Yook, S., Thompson, D. W. J., and Solomon, S.: Climate Impacts and Potential Drivers of the Unprecedented Antarctic Ozone Holes of 2020 and 2021, Geophys. Res. Lett., 49, e2022GL098064, https://doi.org/https://doi.org/10.1029/2022GL098064, 2022.

Yu, P., Davis, S. M., Toon, O. B., Portmann, R. W., Bardeen, C. G., Barnes, J. E., Telg, H., Maloney, C., and Rosenlof, K. H.: Persistent stratospheric warming due to 2019–2020 Australian wildfire smoke, Geophys. Res. Lett., 48, e2021GL092609, 2021.

Zhang, R., Leu, M., and Keyser, L. F.: Hydrolysis of N2O5 and ClONO2 on the H2SO4/HNO3/H2O ternary solutions under stratospheric conditions, Geophys. Res. Lett., 22, 1493–1496, 1995.

Zhu, Y., Toon, O. B., Kinnison, D., Harvey, V. L., Mills, M. J., Bardeen, C. G., Pitts, M., Bègue, N., Renard, J. B., Berthet, G., and Jégou, F.: Stratospheric Aerosols, Polar Stratospheric Clouds, and Polar Ozone Depletion After the Mount Calbuco Eruption in 2015, J. Geophys. Res.-Atmos., 123, 12,308-12,331, https://doi.org/10.1029/2018JD028974, 2018.